



**Politecnico
di Torino**

Master Thesis in Electrical Engineering

ISI-OBC Advanced Modeling and Validation

Supervisor

Prof. Gianmario Pellegrino

Author

Leonardo Longega

Advisor

Paolo Pescetto

July 5, 2023

Contents

| | | |
|----------|--|-----------|
| 1 | Introduction | 1 |
| 1.1 | Vehicle Electrification Scenario | 1 |
| 1.2 | Classification of Chargers and main configurations | 4 |
| 1.3 | The FITGEN project | 7 |
| 1.4 | Motivation and Goal of the Thesis | 8 |
| 1.5 | Integrated Semi Isolated On Board Charger | 9 |
| 2 | PLECS Model of the DC/DC Converter | 12 |
| 2.1 | Simplified Model of the DC/DC stage | 12 |
| 2.1.1 | Waveforms calculation | 12 |
| 2.1.2 | Mean Power Calculation | 17 |
| 2.2 | PLECS blocks and equations | 18 |
| 2.3 | DC/DC stage control | 25 |
| 2.3.1 | Hysteresis control on d axis | 25 |
| 2.3.2 | Hysteresis control on q axis | 26 |
| 2.3.3 | Hysteresis control on alpha or beta axis | 26 |
| 2.3.4 | Sinusoidal voltage control | 27 |
| 3 | Experimental testing and model calibration | 28 |
| 3.1 | Test set up | 28 |
| 3.1.1 | Power components | 30 |
| 3.1.2 | Measurement instrumentation | 31 |
| 3.2 | Measurement of the leakage inductance | 31 |
| 3.3 | Experimental results in alpha axis control | 34 |
| 3.3.1 | Sensitivity to V_h and I_h | 40 |
| 3.4 | Experimental results in d axis control | 42 |
| 3.4.1 | Sensitivity to V_h | 46 |
| 3.5 | Calibration of the PLECS model | 48 |

| | | |
|----------|---|-----------|
| 4 | Simulation Campaign | 52 |
| 4.1 | Control refinements | 52 |
| 4.1.1 | Maximum Id issue not complying with I_h limit | 52 |
| 4.1.2 | Feed forward on q axis | 53 |
| 4.2 | Parametric Analysis | 54 |
| 4.2.1 | Automation | 54 |
| 4.2.2 | Sensitivity to V_h and I_h | 55 |
| 4.2.3 | Angle influence on charging | 57 |
| 4.2.4 | Sensitivity to Vdc1 and V_h | 58 |
| 4.3 | New proposed CC control technique | 61 |
| 4.3.1 | Description of the Control Technique | 61 |
| 4.3.2 | Control calibration | 62 |
| 4.3.3 | Simulation Results | 64 |
| 4.3.4 | Constant Voltage Results | 66 |
| 4.4 | Iron losses of the electrical machine | 67 |
| 5 | Conclusions | 72 |

List of Figures

| | | |
|------|---|----|
| 1.1 | Electric car sales reported by IEA | 1 |
| 1.2 | iOBC configurations | 5 |
| 1.3 | Powertrain traction configuration | 9 |
| 1.4 | Powertrain charging configuration | 10 |
| 2.1 | Voltage vectors of 3-ph inverter | 13 |
| 2.2 | DC/DC stage circuit with v and w phases in parallel | 14 |
| 2.3 | DC/DC stage simplified circuit | 14 |
| 2.4 | Voltage, current and power waveforms at low duty cycle | 15 |
| 2.5 | Voltage, current and power waveforms at high duty cycle | 16 |
| 2.6 | Voltage, current and power waveforms where i_1 takes more time periods to pass the maximum I_h | 17 |
| 2.7 | Isolated DC/DC converter PLECS model | 19 |
| 2.8 | Inverter PLECS block | 20 |
| 2.9 | Rectifier PLECS block | 20 |
| 2.10 | Electric phase voltage and current | 21 |
| 2.11 | Electric motor calculation procedure | 22 |
| 2.12 | Motor blocks | 23 |
| 2.13 | Motor blocks | 23 |
| 2.14 | Motor blocks | 24 |
| 2.15 | Motor blocks | 25 |
| 2.16 | Hysteresis control scheme | 26 |
| 3.1 | Photo of the laboratory workbench | 29 |
| 3.2 | Laboratory instrumentation and interaction | 30 |
| 3.3 | Inductances of the electric motor | 32 |
| 3.4 | Inductances of the electric motor, circuit simplification | 32 |
| 3.5 | Inductances of the electric motor, circuit simplification | 32 |
| 3.6 | Voltage waveforms of primary side in alpha axis control | 36 |
| 3.7 | Current wave-forms of primary side in alpha axis control | 37 |
| 3.8 | Current wave-forms of secondary side in alpha axis control | 37 |

| | | |
|------|---|----|
| 3.9 | Power wave-forms in alpha axis control | 38 |
| 3.10 | Voltage of primary side in alpha axis control in alpha-beta frame | 38 |
| 3.11 | Current in alpha axis control in alpha-beta frame | 39 |
| 3.12 | Angle waveform in alpha axis control | 39 |
| 3.13 | Power in input and output and efficiency at 560V in, 495V out with alpha control | 41 |
| 3.14 | Voltage waveforms of primary side in dq control | 43 |
| 3.15 | Current waveforms of primary side in dq control | 43 |
| 3.16 | Current waveforms of secondary side in dq control | 44 |
| 3.17 | Power waveforms in dq control | 44 |
| 3.18 | Voltage in dq frame in dq control | 45 |
| 3.19 | Current in dq frame in dq control | 45 |
| 3.20 | Power in input and output at 250V in, 200V out with d control | 46 |
| 3.21 | Efficiency at 250V in, 200V out with d control | 47 |
| 3.22 | Angle in measurement at 250V in, 200V out with d control . . | 47 |
| 3.23 | PLECS Voltage in input at 100V in, 70V out, 60V Vh | 49 |
| 3.24 | Experimental Voltage in input at 100V in, 70V out, 60V Vh . | 49 |
| 3.25 | PLECS Current at 100V in, 70V out, 60V Vh | 50 |
| 3.26 | Experimental Current at 100V in, 70V out, 60V Vh | 50 |
| 3.27 | PLECS Power at 100V in, 70V out, 60V Vh | 51 |
| 3.28 | Experimental Power at 100V in, 70V out, 60V Vh | 51 |
| 4.1 | Parametric analysis procedure | 55 |
| 4.2 | Vh and Ih influence at 400V, 550V in out with d control . . . | 56 |
| 4.3 | Vh and Ih influence at 400V out, 550V in with d control . . . | 56 |
| 4.4 | Vh and Ih influence at 400V out, 550V in with d control . . . | 57 |
| 4.5 | Angle influence at 550V in, 400V out, 150V Vh with d control | 58 |
| 4.6 | Vh and V1 influence at 400V out with d control | 59 |
| 4.7 | Vh and V1 influence at 400V out with d control | 60 |
| 4.8 | Vh and V1 influence at 400V out with d control | 60 |
| 4.9 | Battery charging current control loop | 61 |
| 4.10 | Battery charging current control loop | 63 |
| 4.11 | Battery current control at 400V battery voltage | 65 |
| 4.12 | Battery current control at 400V battery voltage | 65 |
| 4.13 | Battery current control CC and CV | 66 |
| 4.14 | Iron losses 3D plot | 69 |
| 4.15 | Iron losses 2D plot | 69 |
| 4.16 | Vh and V1 influence at 400V out with d control considering iron losses | 70 |

List of Tables

| | | |
|-----|--|----|
| 1.1 | Requirements and standards | 6 |
| 3.1 | Leakage inductance measures | 34 |
| 4.1 | Results comparison $V_{in} = 100V$, $V_{out} = 70V$, $V_h = 60V$ | 71 |
| 4.2 | Results comparison at $V_{in} = 250V$, $V_{out} = 200V$, $V_h = 160V$. | 71 |

Chapter 1

Introduction

1.1 Vehicle Electrification Scenario

The last few years have seen the worldwide spread of electric vehicles as reported by the International Energy Agency (IEA) [1], as shown on the Figure 1.1.

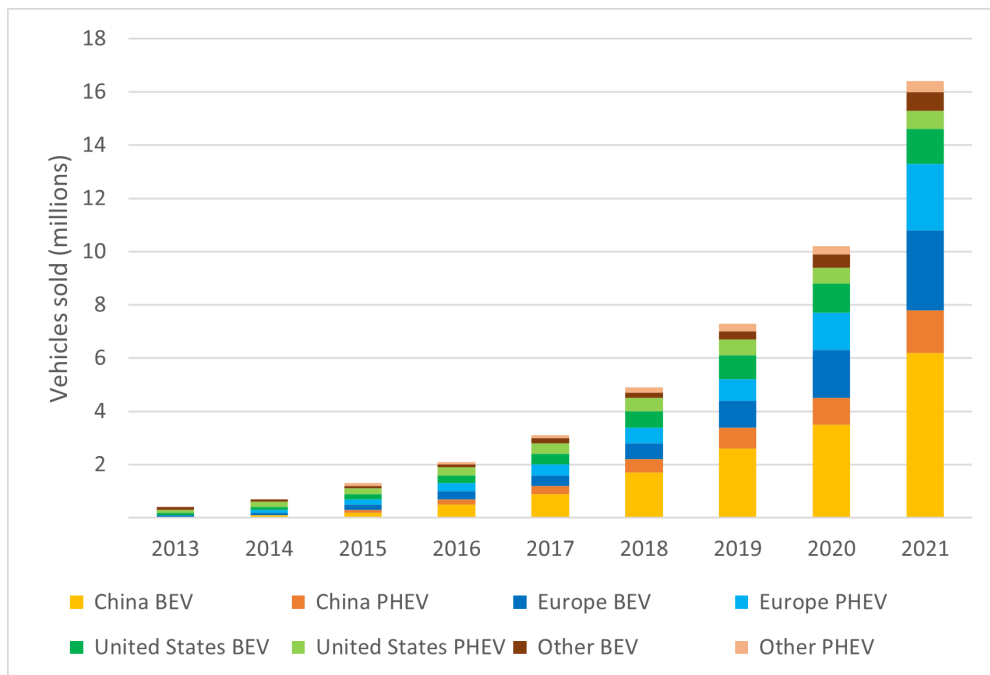


Figure 1.1: Electric car sales reported by IEA

The forecasts for future years made by various institutions predict a prosecution of the present trend leading to a massive spread of electric vehicles.

Examples of forecasts are the following:

- Accordingly to International Renewable Energy Agency (IRENA), by 2050 around 70% of all cars, buses, two- and three-wheelers and trucks will be powered by electricity [2].
- The IEA Announced Pledges Scenario (APS), presumes that EVs represent more than 30% of vehicles sold globally in 2030 across all modes (excluding two- and three-wheelers). The IEA Stated Policies Scenario (STEPS), EVs reach over 20% of sales in 2030 [3].
- The MIT report “Insight into Future Mobility” forecasts a Global EV share of Light-duty vehicles of 33%, 38% and 50% respectively for the Reference, Paris Forever and Paris to 2°C scenarios [4].

Depending on the models and on the environmental policies considered the results differ, in any case the scenarios predict an increase in the sale of electric vehicles in the future.

The main cause that is driving the spread of electric vehicles is related to pollution and climate change. During the COP21 with the Paris Agreement [5], measures were approved, ratified by most countries, to promote sustainable development, reduce greenhouse gas emissions and limit climate change by aiming to keep the global average temperature increase at the end of the century below 2°C compared to pre-industrial era. As a result of the measures adopted during COP21, a European directive followed, leading each EU state to draw up detailed national plans with the main goal of achieving climate neutrality by 2050 [6], [7]. Some of the measures to reduce this target are to increase the use of renewable resources, increase energy efficiency and increase the interconnection of the electricity grid between member states. To achieve these goals, the solution is the energy transition, i.e. replacing the fossil-fuel based energy system with a low- or zero-emission one based on renewable resources. It is clear that electric cars represent an enabling technology and a key element in achieving the energy transition. EVs make it possible to keep city centres unpolluted to the benefit of citizens’ health, they enable the exploitation of energy produced from renewable sources for mobility and they can also provide grid services, when connected via V2G, which will be further crucial for grid stability as RES is scaled up. Another important reason why a transition to electric power is necessary in the coming years concerns the depletion of fossil reserves. In fact, according to data from BP (formally called The British Petroleum Company plc) published in the report “Statistical Review of World Energy 2021” [8], the time remaining before the depletion of world reserves (calculated as the ratio of proven

reserves over the production in 2020) of oil, natural gas and coal is 53.5, 48.8 and 139 years respectively.

The supply of fossil fuels is affected by geopolitical frictions between countries and in some cases it can also be the cause. Examples are the Yom-Kippur war of 1973 which led to the first energy crisis, the Iranian revolution of 1979 which resulted in the second energy crisis, a current example concerns the complications and price rises in the supply of natural gas in Europe during the war between Russia and Ukraine as well as in the past there had already been tensions in relation to the supply of natural gas. In addition, the inevitable depletion of fossil resources could intensify geopolitical tensions and therefore needs to be prevented by a successful energy transition.

The exhibited causes for the need of the energy transition are known not only to ecologists, but gradually are becoming part of the collective consciousness. Consequently, in order to create a sustainable economy, are being created new job opportunities and new market sectors, including electric vehicles, as the consequence of public and private investments.

The development of battery technology plays a key role in increasing the range autonomy of vehicles and overcoming the range anxiety of the customers. At the same time much research is being done on charging systems to reduce charging time while preserving the battery life.

The market for electric vehicles is growing, but until a few years ago the production volumes were still quite small and as a result car makers preferred to buy individual components such as power electronic converters and electric motors to assemble inside the vehicles because it was not worth the expense and there was no time to better equip in-house.

As production volumes increase, however, more and more effort is being made to cut costs and thus integrate components with more effort into systems solution rather than single components. Some examples are the following:

- Tesla is an example of a factory that produces its own components in order to reduce the costs and avoid problems with the sellers.
- The Volkswagen Technology called "Modularer E-Antriebs-Baukasten" (MEB) that is the German name of modular electric drive matrix [9], it is a scalable module of the whole powertrain that is the basis for 27 vehicle models in 2022.
- The "Advanced driving module" by Bosch [10] is a highly integrated electric axis.

- The FITGEN Project [11] aims at developing a brand-independent functionally integrated e-axle, it is explained on a dedicated section.

This Thesis is related to this framework of research and innovation, more specifically with regard to innovative On-Board Chargers.

1.2 Classification of Chargers and main configurations

Battery charging in plug-in hybrids (PHEVs) and BEVs is divided into slow charging or AC charging, and fast charging or DC charging. There are also alternatives ways of charging but are uncommon, such as the wireless charging.

The on-board charger allows the vehicle to connect directly to an AC single or three phase. The off-board chargers instead provide already a DC voltage and are usually installed in dedicated charging stations allowing higher powers with respect to on-board chargers [20], the infrastructure cost is higher but the charger can be exploited by many customers.

The standard for conductive charging in Europe is the IEC 61851-1. It distinguish 4 charging modes:

- Mode 1: Home
Immediate personal charge of road vehicles at home or in private places in AC, there are some limitations as the power level between 1 and 4 kW and doesn't allow V2G.
- Mode 2: Mode 3 to Mode 1
It allows to use Mode 1 on Mode 3 plugs without a real charging station.
- Mode 3: Energy marketing
Adopted by public charging stations, it allows to charge in AC at power levels typically up to 22kW or higher in 3-phase.
- Mode 4: DC charge
It exploit an off-board charger, placed on the charging station, to charge the battery in DC with high power levels.

This standard, the IEC 61851-1, also defines the physics connections such as sockets and plugs, electric specifications as voltage and power levels, the communication protocol for Vehicle to Grid (V2G).

Another distinction is between unidirectional and bidirectional power flow capability. Unidirectional charging reduces hardware requirements and simplifies interconnection with the grid while bidirectional charging allows power injection back to the grid and provide grid ancillary services through V2G.

The OBC can adopt standalone or integrated configurations. As explained before, during the initial EVs spreading are preferred standalone OBCs than integrated OBCs because of their small volume of production. In order to reduce the costs of production the producers are moving toward integrated solutions as aimed by the FITGEN Project [11]. Actually most of the EV employs standalone on-board chargers that are unidirectional and in some cases also bidirectional but usually exploited as unidirectional because of the lack of V2G full development. Various topologies and control schemes of on-board chargers have been presented in [12], [14], [15], [16]. In order to overcome the limitations of on-board battery chargers (OBCs) while preserving their advantages, the integrated OBCs exploit existing propulsion circuit components, the electric motor and the inverter, for battery charging instead of a separate charging circuit with bulky additional inductors and transformer. The motor windings are used as filter inductances or as galvanic isolation. While the propulsion inverter is used as a bidirectional DC/AC converter. The effectiveness of this technique demands some technical requirements as galvanic insulation and zero torque production during the charging. Achieving these desirable features will highly depend on the motor type, number of phases, and employed power converter. The electric motor types utilized in EVs include induction motors, permanent magnet machines, and switched-reluctance motors. According to the analysis of battery electric vehicles (BEVs) introduced in [17], the PMSM is the most commonly used in current BEVs. There are therefore several possible configurations of iOBC, in order to provide a clear panoramic it is shown the Figure 1.2.

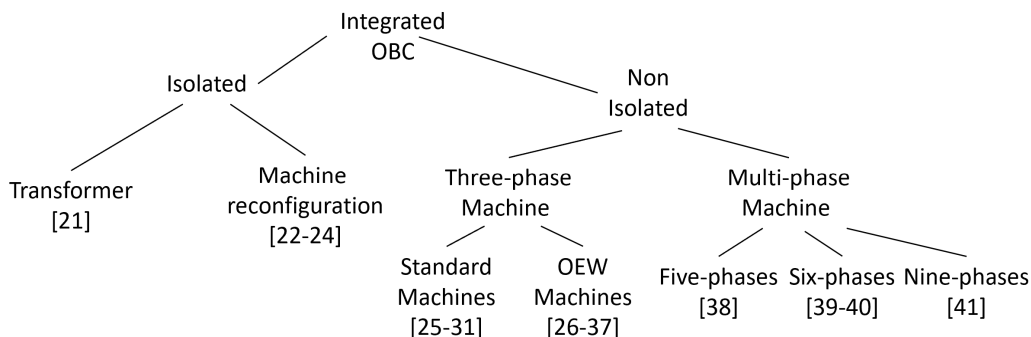


Figure 1.2: iOBC configurations from [14]

Non-isolated i-OBCs are the majority, as can be seen in the Figure 1.2; the lack of galvanic isolation, however, is a highly penalising factor as it negatively affects safety. Configurations for insulated iOBCs, on the other hand, are rare, and the articles dealing with such configurations are also scarce. The former can be divided into converters that require an additional transformer, which is penalising factor as it is bulky and heavy, whereas others use the electric motor reconfigured as a transformer. The iOBCs that exploit the reconfigured motor as a transformer reported in the literature are mainly of two types: Isolated Full Integrated On-Board Charger (IFI-OBC) [18] and Isolated Semi-Integrated On-Board Charger (ISI-OBC) [19]. These converters involve a high level of integration of existing components in EVs with 6-ph PMSM. The main disadvantage of the IFI-OBC is that the motor, being connected to the grid, does not operate at nominal flux and consequently a reconfiguration of the number of windings is required to avoid saturation, a complication that is not widely accepted by vehicle manufacturers. The ISI-OBC, on the other hand, requires an additional diode bridge and grid-side filter inductances, although this configuration allows the considerable advantage of adjusting the motor excitation frequency and consequently also the magnetic flux by acting directly on the inverter.

The battery chargers need to comply with standards. The standards of interest concerning the conductive charging of electric vehicles are the CEI EN 61851-1 and the CEI EN 61851-21-1. The key information of the standards and the main requirements for the OBCs are collected on the Table 1.1.

| | |
|---|---|
| <p>Grid side constraints: current waveform (THD<5%) power factor >0.95 V2G capability</p> | <p>Battery constraints: battery current regulation battery voltage regulation</p> |
| <p>Motor constraints: no torque production no PM demagnetization minimal winding reconfiguration</p> | <p>General requirements: high efficiency (reduced losses) galvanic insulation minimal (or no) additional hardware single and three phase operation</p> |

Table 1.1: Requirements and standards

1.3 The FITGEN project

The FITGEN project [11], financed by the European Union, started in early 2019 aiming to develop a brand-independent functionally integrated e-axle for EVs, to be tested on a full electric vehicle demonstrator. Thanks to the cooperation between academic and industrial partners, the project targets high innovation and technology readiness level, for mass production third generation EVs. In particular, the e-Axle under development([11], [13]) is equipped with a 6-phase Buried Permanent Magnet Synchronous Motor (BPMSM) supplied by high efficiency Silicon-Carbide (SiC) inverter and a high-speed transmission gearbox. The 6-phase inverter is connected to the battery through a DC/DC converter, elevating the battery voltage (rated 400 V) to a maximum of 750 V, to ensure high dynamic performance at high speed as well as embedded fast and super-fast charging capabilities. The FITGEN project aims to improve the existing EVs technology respect to the 2018 state of the art in three main aspects:

- Power electronics and charger: the power density will be increased by 50% thanks to the adoption of the latest SiC power MOSFET components, reaching a peak efficiency of 99% and ensuring embedded charging and super-fast charging capability.
- Electric motor and transmission: the target is increasing the gravimetric power density by 40% thanks to a high-speed Buried Permanent Magnet-Synchronous Machine (BPMSM), deeply integrated with a compact single-speed transmission.
- Cooling and control: several solutions of cooling system are under investigation, including a strongly optimized liquid cooling system for the machine and converters functionally integrated with the oil cooling system required for the transmission gearbox. A joint control of the SiC inverter and the DC/DC converter is under development, enabling high-voltage operation of the e-motor during traction mode.

The latest advances of the FITGEN Project are collected in [13], it confirms a strong improvement of the e-Axle performances with respect to the 2018 state of the art.

This Thesis is related to the European project FITGEN, PoliTO is one of the academic contributors to the project. Among the other tasks, PoliTO is required to evaluate innovative solutions for On-board Battery Chargers (OBC), and in particular possible integration of the OBC with the traction drive. At the present status of the work, several possible topologies

for isolated IOBCs have been simulated using PLECS, and a traction synchronous motor is available for experimental validation. The contribution of this Thesis regarding the simulations is to provide a realistic PLECS simulation model of the DC/DC in order to provide an evaluation of the operation of the ISI-OBC in every possible working point. Furthermore are carried out experimental validations of the integrated charger on the 6-phase traction drive at a full load of 6 kW 1ph and 10 kW 3ph also emulating the battery behavior.

1.4 Motivation and Goal of the Thesis

This Thesis is committed to the study, modelling and testing of a proof-of-concept Isolated Semi-Integrated On-Board Charger (ISI-OBC). It is obtained from a traction drive with a hexaphase electric machine and a dual three-phase inverter.

The Thesis firstly studies the PLECS model of the DC/DC converter with a 6-phase motor as transformer.

Subsequently, an experimental phase takes place to obtain losses and efficiency data to improve the PLECS model. This part comprises:

- full power experimental validation of the ISI-OBC, with single-phase and three-phase power supply to verify control quality and waveforms, with various zero torque control techniques;
- measurement of the efficiency of the AC/AC side, and also of the two power converters;
- characterisation of losses in the iron and magnets of the high-frequency excited machine to improve the PLECS model by including losses.

The PLECS model of the AC motor is then improved, including high frequency losses, uniformly to the syreDrive standard.

The final goals of the thesis are:

- obtain a complete model of the ISI-OBC both in single-phase and in three-phase charging modes;
- experimentally validate ISI-OBC at full load, i.e. 6 kW single-phase and 10 kW three-phase at constant battery voltage;
- defining and testing the most effective control technique in terms of minimising vibration, maximising charging efficiency and safety;

- the determination of the theoretical efficiency limit of the integrated or semi-integrated solution, compared to the efficiency of a reference standalone OBC.

1.5 Integrated Semi Isolated On Board Charger

In order to allow the configuration ISI-OBC the EV should employ a 6-ph PMSM. It is a restrictive requirement but the PMSM is the most used in EVs and with the increase of the power of EVs for a better management and reliability can be used a double 3-ph motor for splitting and better manage the currents. Then for traction mode it is considered the powertrain topology shown on Figure 1.3.

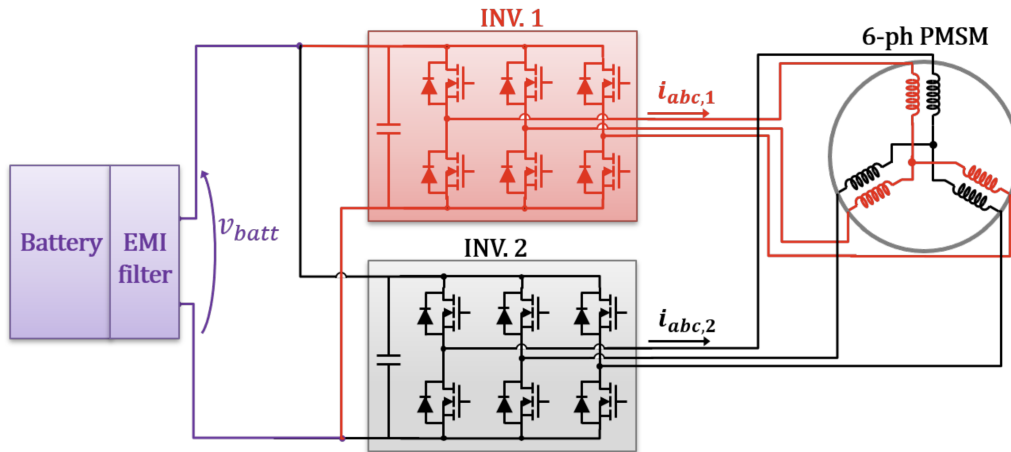


Figure 1.3: Powertrain traction configuration from [19]

On the charging-mode configuration the topology of the charging system is shown on Figure 1.4.

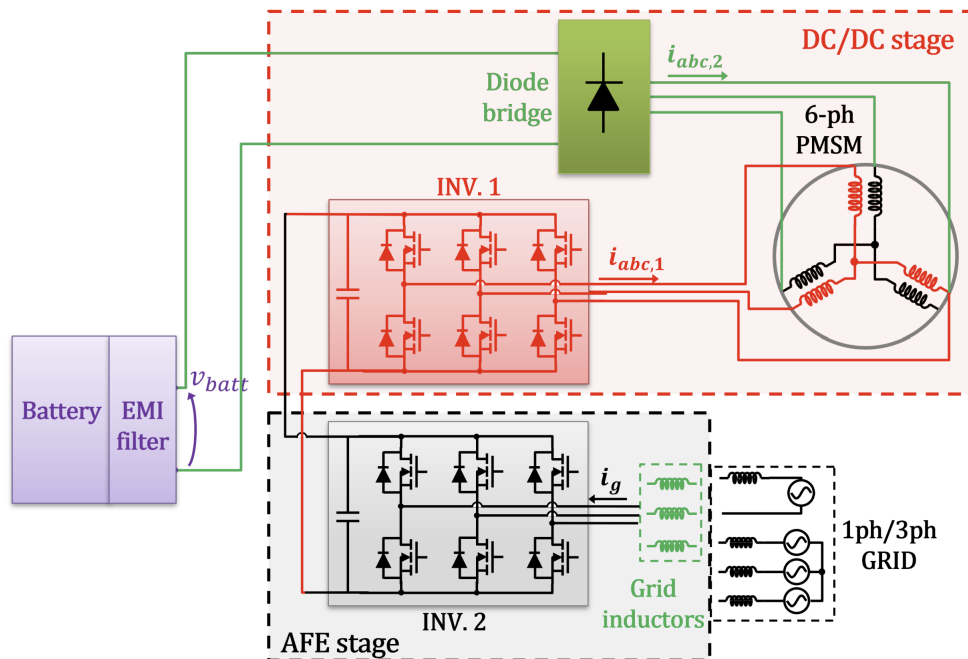


Figure 1.4: Powertrain charging configuration from [19]

The PMSM is exploited as an HF transformer, allowing the galvanic insulation of the battery from the inlet grid. The excitation frequency is freely imposed by the inverter in order to be compatible with the PMSM ratings avoiding magnetic saturation. In charging mode the two inverters keep sharing the DC-link but this is disconnected from the battery. On the 3-ph side, one inverter is connected to the grid through grid filtering inductors and works as an Active Front End (AFE); the second inverter excites the PMSM on a 3-ph set providing a square wave voltage, regulating the power transfer and avoiding torque production. The other 3-ph set of the PMSM are connected to a diode bridge to rectify the current to the battery. On this configurations the components must work complying with their specifications. Usually the rated power of the converters and motors is higher than the charging power and then can be suitable for the charging-mode.

AFE Stage

The inverter connected to the grid is used for rectifying the grid voltage. It works as an Active Front-End (AFE) rectifier, the purpose is to guarantee sinusoidal grid current with unitary power factor, and to provide a stable DC-link to supply the second inverter. The grid connection requires filtering inductors to control the grid current with a low THD. The number and size of such inductors depend on the required OBC power level and grid inlet if

3-ph or 1-ph.

Isolated DC/DC Stage

The core of the ISI-OBC topology is to use the traction motor as an HF isolation transformer in the DC/DC stage. The connection of the inverter to the motor windings is not modified respect to the traction configuration. This inverter is employed to regulate the power to the battery exciting the PMSM with a square wave voltage with a proper frequency in order to be similar to the rated value during traction, to avoid magnetic saturation and also to avoid torque at the shaft. The second set of windings undergo an induced voltage since is magnetically coupled with the first set of windings that is excited by the inverter. The second set of windings is connected to a diode bridge and then to the battery. The current flow is the result of the voltage difference between the rectified voltage and the battery voltage, the current variation is limited by the circuit resistances and inductances.

Chapter 2

PLECS Model of the DC/DC Converter

Figure 1.4 shows the charging configuration. Inside the grey block it is shown the AFE stage that is a standard converter. Meanwhile in the red block the DC-DC stage is comprehended and is the one that is examined in detail in this section.

2.1 Simplified Model of the DC/DC stage

In order to understand the operation of the converter and to better understand the results obtained from simulations and experimental tests, a new simple theoretical model of the DC/DC stage of the iOBC is realised that wasn't available before. In addition, this section will later be useful for the implementation of a control to regulate the charging current on the battery side.

2.1.1 Waveforms calculation

The first type of control considered is the d-axis hysteresis control which will be explained in detail later. This type of control is based on a hysteresis mechanism which imposes a voltage in the d-axis called the hysteresis voltage V_h whose sign is varied each time the control detects that the current in the d-axis exceeds the current called the hysteresis current I_h . On the q-axis, on the other hand, a PI controller with zero current reference is used in order to minimise torque production. The voltage V_h is regulated in PWM and the maximum amplitude is variable and depends on the position of the rotor. This is due to the fact that the voltage vectors that the 3-ph inverter can

instantaneously supply are 6, the vertices of which form the hexagon shown in Figure 2.1.

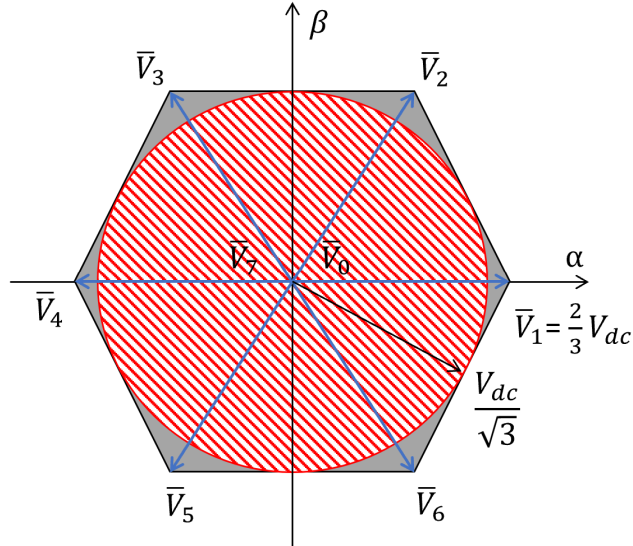


Figure 2.1: Voltage vectors of 3-ph inverter

The average voltages that can be supplied by the inverter are all the points belonging to that hexagon but since the perimeter points have varying distances from the centre, in the different directions the maximum voltage limit is variable between $V_{dc}/\sqrt{3} = V_{dc} * 0.577$ and $V_{dc} * 2/3 = V_{dc} * 0.66$.

As the Clarke matrix used is in the form that maintains the amplitudes of the vectors in abc and dq coordinates, the explained voltage limits are the same in the reference dq and thus for the hysteresis voltage V_h .

To analyse the DC/DC stage, it is considered the rotor aligned with the a-axis. In this case, the axes a, d and alpha are the same. This is a specific case that allows for simpler waveforms than a generic rotor position. In this case, the direction of the rotor is the same as two of the hexagon's voltage vectors, and therefore the choice of how to operate the switches is straightforward as it does not require modulation between two different vectors at different angles. With the further simplification of neglecting q-axis control, it is possible to connect phases b and c in parallel as can be seen in Figure 2.2.

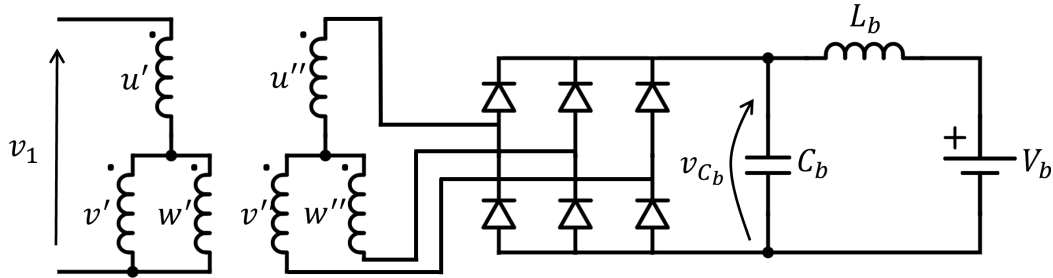


Figure 2.2: DC/DC stage circuit with v and w phases in parallel

Starting from the circuit shown in Figure 2.2, considering that the phases b and c at secondary correspond to the phases in parallel in the primary and then that they behave in the same way, also the secondary b and c phases can be put in parallel. Therefore, neglecting the magnetising inductance and calculating the equivalent leakage inductance shown at primary, the circuit shown in Figure 2.3 is obtained.

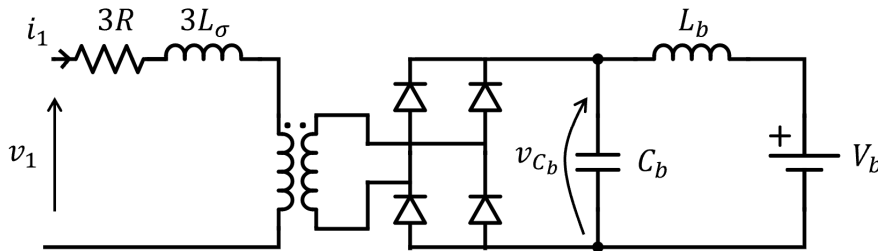


Figure 2.3: DC/DC stage simplified circuit

From the circuit in Figure 2.3, the voltage and current waveforms at the various points of the circuit and the power were obtained.

It is assumed that the capacitor voltage on the battery side in a PWM period has an approximately constant voltage because it is assumed that it filters the voltage well. Then considering the voltage waveforms and the differential inductor Equation 2.1 rewritten as in Equation 2.2, the waveforms obtained are shown in Figures 2.4, 2.5 and 2.6. In Equation 2.2 the inductance is replaced with the equivalent leakage inductance and the voltage applied to it is the difference between the input and output voltages.

$$v_L(t) = L \frac{di(t)}{dt} \quad (2.1)$$

$$i(t) = \int_0^t \frac{v_L(t)}{L} dt \quad (2.2)$$

In Figure 2.4, a low hysteresis voltage V_h is considered which causes the current within the period to annul. The maximum current is considered to exceed the hysteresis current I_h and thus the sign of V_h is inverted each period.

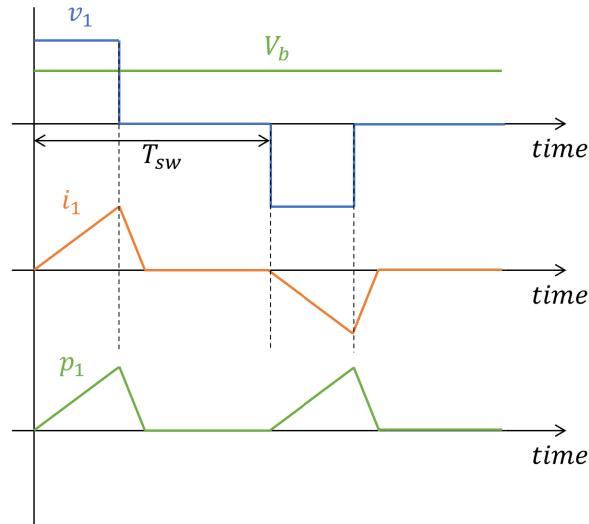


Figure 2.4: Voltage, current and power waveforms at low duty cycle

In Figure 2.5, a high value of V_h is considered, which causes the voltage V_h to have to force the current to zero before reversing its sign and thus causing negative power peaks. Here as well, a period is assumed to be sufficient to exceed the value I_h .

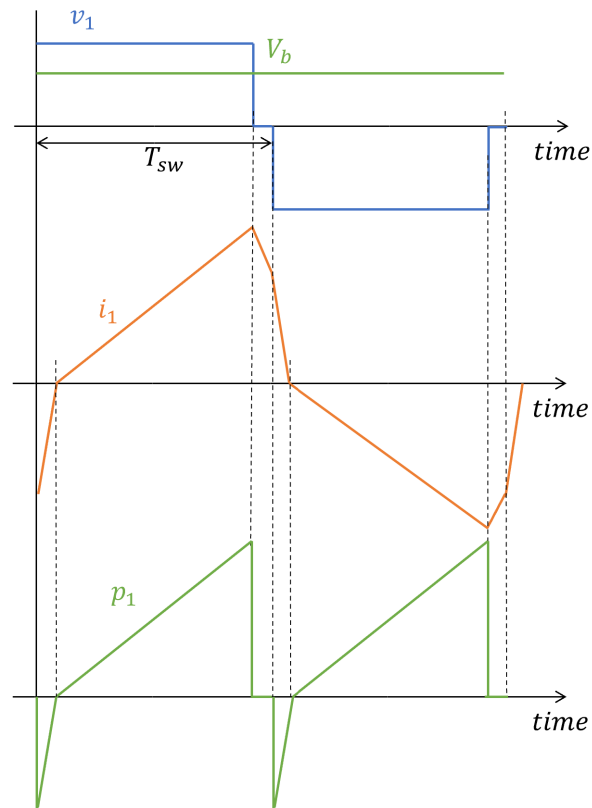


Figure 2.5: Voltage, current and power waveforms at high duty cycle

The last case considered is the one shown in Figure 2.6. A high value of V_h is considered but differently from the previous case, two PWM periods are required to exceed the threshold I_h .

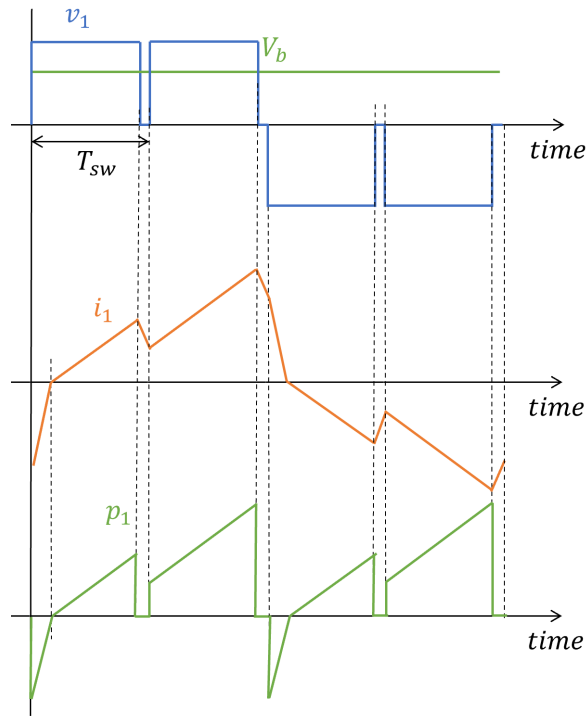


Figure 2.6: Voltage, current and power waveforms where i_1 takes more time periods to pass the maximum I_h

In Figures 2.5 and 2.6, because the voltage reverses before the current cancels, and because power is the result of the product voltage times current, there are negative power peaks that correspond to the recovery of energy stored in the magnetic field.

2.1.2 Mean Power Calculation

The only time periods in which power is provided is when both current and voltage are present at the same time, and thus when voltage v_1 is different from zero. The waveform of the current in the time period when voltage is supplied is a ramp. Consequently, the average power in the PWM period is calculated as in Equation 2.3.

$$P_{mean-T} = \frac{1}{2}(i_{pk} - i_0)V_1d = \frac{1}{2}((i_{pk} - i_0)\frac{3}{2}V_h) \quad (2.3)$$

In Equation 2.3 the i_0 and i_{pk} are respectively the alpha current at the beginning of the PWM period and the peak.

With an approximation, considering a single current ramp between periods until reaching the maximum value and reversing the polarity of the

voltage, the Equation 2.4 is obtained. For the calculation of average power, the time it takes for the current to reverse is neglected, as these are time intervals in which the derivative of current is much greater than the rest, and are therefore short periods of time.

$$P_{mean} = \frac{1}{2}I_{max}V_1d = \frac{1}{2}I_h\frac{3}{2}V_h \quad (2.4)$$

The result of this calculation is that the power is strictly dependent and is proportional to the control variables hysteresis current I_h and hysteresis voltage V_h . However, it is necessary to consider the result of the experimental tests and the model in order to understand the actual behaviour of the converter.

The Section 2.1 will be useful also for the calculation of the dynamics behavior of the DC/DC stage needed for the battery current control strategy developed in the later Section 4.3.

2.2 PLECS blocks and equations

In PLECS, in order to model the DC-DC stage, the components inside the converter are shown in Figure 2.7. From left to right are present:

- a constant voltage generator, inductor and capacitors represent the dc-link of the AFE
- an inverter and its control block, the element which serves to control the charging and which produce AC voltage waves to the motor
- the 6-ph electric motor used as a transformer
- a diode bridge that rectifies the motor's secondary voltage and also incorporates an LC filter to reduce battery-side current ripple
- a constant voltage output representing the battery to be charged

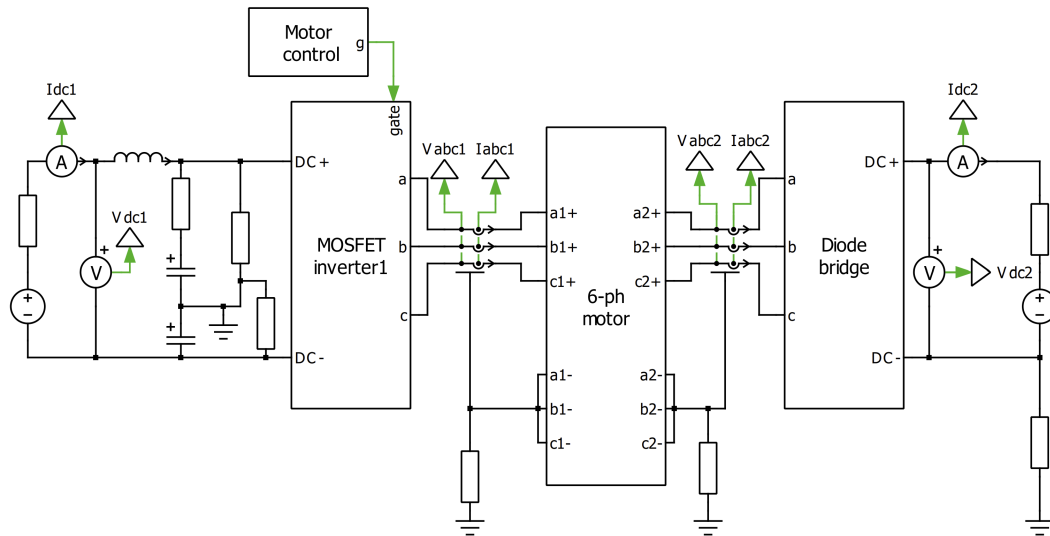


Figure 2.7: Isolated DC/DC converter PLECS model

The inverter block "MOSFET inverter1" is shown in Figure 2.8. It is realised using MOSFETs made available by PLECS. The inverter block receives the gate signals of the individual switches from the "Motor control" block shown in Figure 2.7. The "Motor control" block has several inputs consisting of all the measurements that are required to operate the inverter. Using the same C code that was used inside the microcontroller in the lab, the output signals are generated which consist of the gate signals of the MOSFETs.

The "Diode bridge" block shown in Figure 2.9 is also realised using the standard PLECS diode blocks. Figure 2.9 shows the battery-side filter incorporated in the "Diode bridge" block, whose function is to reduce the charging current ripple and thus reduce battery stress.

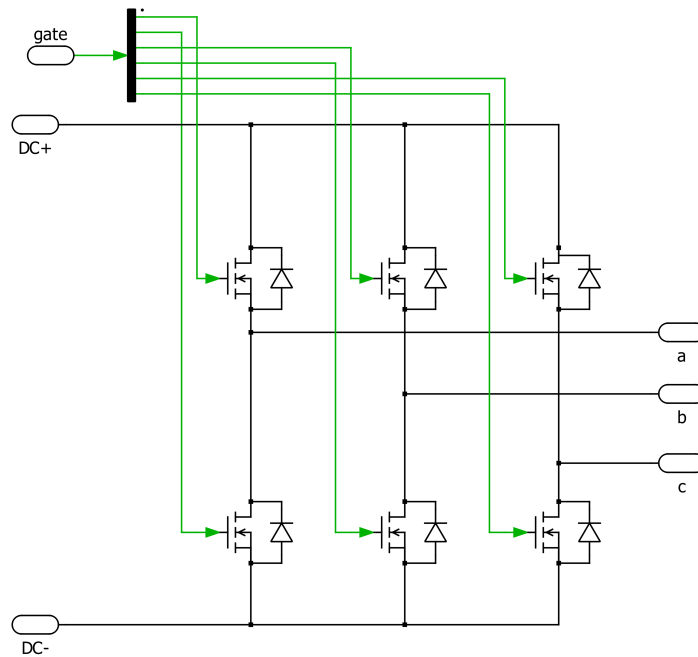


Figure 2.8: "MOSFET inverter1" PLECS block

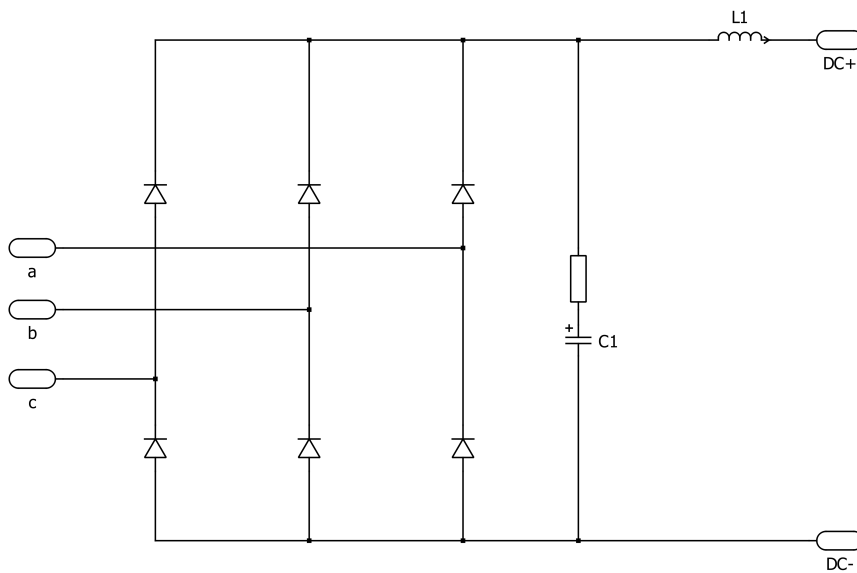


Figure 2.9: "Diode bridge" PLECS block

The electric motor, on the other hand, is modelled in detail, without using the motor or transformer blocks of PLECS. Considering the equations

of the electric motor shown later, its behaviour is modelled in PLECS with mathematical blocks.

In the following it is clarified the procedure and the equations exploited for developing the "6-ph motor" PLECS block.

First of all Figure 2.10 shows that the motor model is based on the phase voltage measurement, while the phase current is imposed based on the motor model.

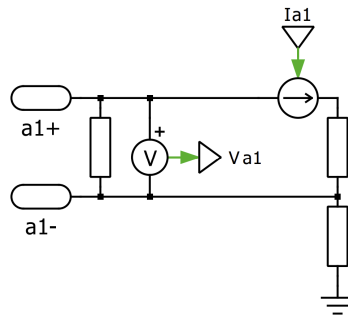


Figure 2.10: Electric phase voltage and current

The "6-ph motor" block elaborating the measured voltage of each phase and considering also the currents itself imposes, it updates the currents through the procedure summarised in the flow chart of Figure 2.11. Every step is explained in detail in the following calculations.

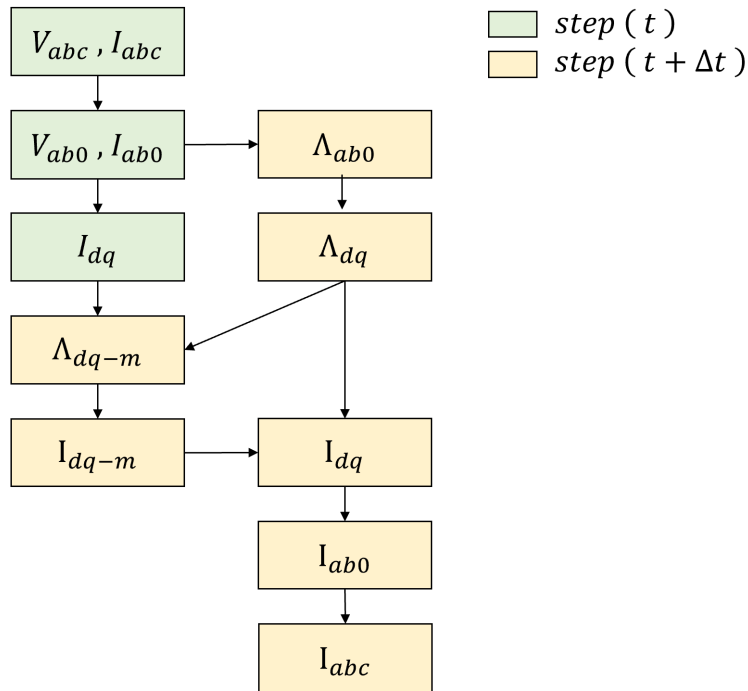


Figure 2.11: Electric motor calculation procedure

Employing the Equation 2.5, the voltages are transferred from the abc axes to the ab0 axes through the matrix T that is calculated in order to maintain unvaried the phasors amplitude. The same procedure is applied for the currents in Equation 2.6.

$$V_{ab0,i}(t) = T * V_{abc,i}(t) \quad (2.5)$$

$$I_{ab0,i}(t) = T * I_{abc,i}(t) \quad (2.6)$$

In order to be able to calculate the magnetic flux of the machine it is used the Equation 2.8 obtained from the Equation 2.7.

$$V_{ab0,i}(t) = R_s * I_{ab0,i}(t) + \frac{d\Lambda_{ab0,i}(t)}{dt} \quad (2.7)$$

$$\Lambda_{ab0,i}(t) = \int (V_{ab0,i}(t) - R_s * I_{ab0,i}(t)) dt \quad (2.8)$$

Employing the rotation matrix $R(\theta)$, in the Equation 2.9 the magnetic flux is brought into dq coordinates and the same is done for the currents in Equation 2.10.

$$\Lambda_{dq,i}(t) = R(\theta)\Lambda_{ab,i}(t) \quad (2.9)$$

$$I_{dq,i}(t) = R(\theta) * I_{ab,i}(t) \quad (2.10)$$

Figure 2.12 shows how the flux in dq axes is obtained from the voltages and currents using Equations 2.5, 2.8 2.9.

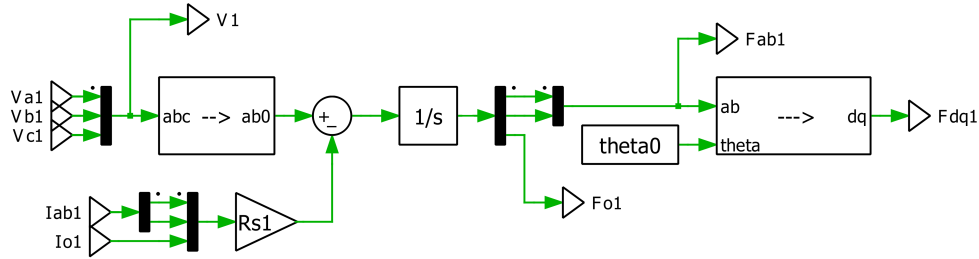


Figure 2.12: Motor blocks

In order to calculate the magnetizing flux it is considered the magnetic circuit of the primary and secondary coils that includes the primary and secondary leakage inductances and the magnetizing inductance. It is then obtained the Equation 2.11.

$$\Lambda_{dq,m}(t) = \frac{1}{2} [\Lambda_{dq,1}(t) + \Lambda_{dq,2}(t) - L_{\sigma} * (I_{dq,1}(t) + I_{dq,2}(t))] \quad (2.11)$$

If the machine had linear behaviour, it would be sufficient to divide the magnetising flux by the magnetising inductance to obtain the magnetising current. In the real case, a non-linear behaviour of the ferromagnetic material occurs and it is necessary to shift to Equation 2.12 due to the non-linearities and use look-up tables that can be obtained through experimental tests or FEM.

$$I_{dq,m}(t) = f_{LUT}(\Lambda_{dq,m}(t)) \quad (2.12)$$

To calculate the magnetising current, Equations 2.11 and 2.12 are used, which are written in PLECS as in Figure 2.13.

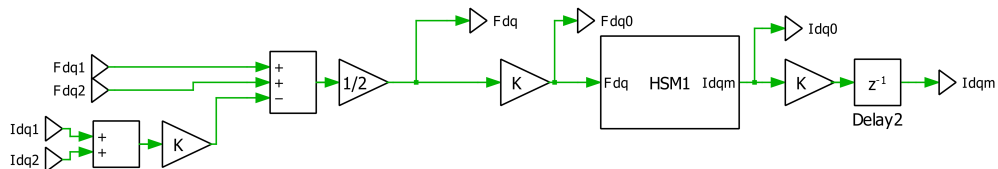


Figure 2.13: Motor blocks

In Figure 2.13 there is a z^{-1} block whose function is to delay the signal by one calculation step. It was introduced to avoid algebraic loops, causing convergence problems for specific simulation tests such as short circuit. This block, however, causes an error in the calculation of the powers and has been removed for simulations in which the iOBC's powers and efficiency are calculated.

At this point, with the new magnetising current known, the primary and secondary currents are recalculated. Using Equation 2.13, subtracting the primary and secondary currents gives Equation 2.14. Then the System of Equations 2.15 is easily obtained.

$$\Lambda_{dq,i}(t) = L_\sigma * I_{dq,i}(t) + L_m * I_{dq,m}(t) \quad (2.13)$$

$$\Lambda_{dq,1}(t) - \Lambda_{dq,2}(t) = L_\sigma(I_{dq,1}(t) - I_{dq,2}(t)) \quad (2.14)$$

$$\begin{cases} I_{dq,1}(t) - I_{dq,2}(t) &= \frac{\Lambda_{dq,1}(t) - \Lambda_{dq,2}(t)}{L_\sigma} \\ I_{dq,m}(t) &= I_{dq,1}(t) + I_{dq,2}(t) \end{cases} \quad (2.15)$$

Solving the System of Equations 2.15 are found the currents in the reference dq of both 3-ph sets (excluding the homopolar component) as shown in Equations 2.16 and 2.17.

$$I_{dq,1}(t) = \frac{1}{2}(I_{dq,m}(t) + \frac{\Lambda_{dq,1}(t) - \Lambda_{dq,2}(t)}{L_\sigma}) \quad (2.16)$$

$$I_{dq,2}(t) = \frac{1}{2}(I_{dq,m}(t) - \frac{\Lambda_{dq,1}(t) - \Lambda_{dq,2}(t)}{L_\sigma}) \quad (2.17)$$

The Equations 2.16 2.17 that allow the calculation of the primary and secondary currents are included in PLECS as in Figure 2.14.

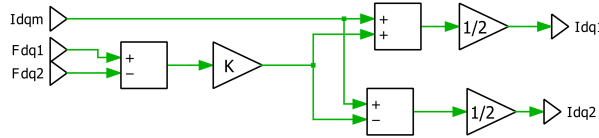


Figure 2.14: Motor blocks

Finally, the currents are calculated back to the abc reference system via Equations 2.18 and 2.19.

$$I_{ab,i}(t) = R^{-1}(\theta) * I_{dq,i} \quad (2.18)$$

$$I_{abc,i}(t) = T^{-1} * I_{ab,i} + \frac{1}{3} \frac{\lambda_{0,i}}{L_\sigma} \quad (2.19)$$

In Equation 2.19 the unipolar component is added.

At this point, the phase currents are calculated from Equations 2.18 2.19 as in Figure 2.15.

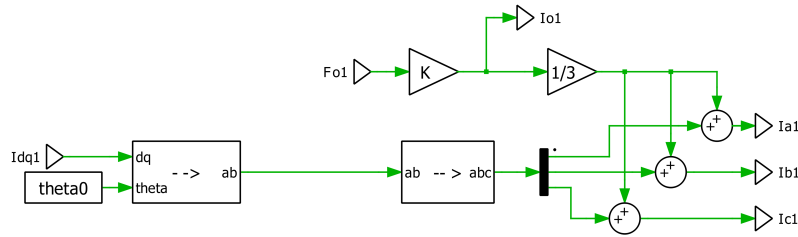


Figure 2.15: Motor blocks

2.3 DC/DC stage control

The purpose of controlling the DC/DC stage is to regulate the charging current of the battery. This is possible by acting on the inverter and thus on the primary voltage modulation. There are several possible control methods and some of these will be illustrated. Each control technique has advantages and disadvantages which will determine the choice of the control technique used. In this case, one of the important elements that will determine the choice is that charging must be carried out by limiting the production of mechanical torque at the shaft in order to avoid considerable vibration and mechanical stress. Furthermore, attention must be directed at flux excitation amplitude and frequency to avoid saturation and limit losses in the iron, to be compatible with the traction specifications. Also the requirements and standards shown before on Table 1.1 need to be considered.

2.3.1 Hysteresis control on d axis

The schematic of the axis control technique is shown in Figure 2.16. In this type of control the mean value of the primary d-axis voltage V_h is regulated in PWM. A maximum current I_h is specified and when it is exceeded, the d-axis voltage polarity is reversed and a hysteresis mechanism follows. The maximum current I_h can be obtained from the flux maps so as not to saturate the machine. The amplitude of the voltage V_h also directly affects the frequency of the excitation since the current has a ramp variation whose

The beta-axis instead fully employ the phases b and c while the phase a maintains null average voltage and just a current ripple.

The alpha-axis control has been considered as a comparison to the results obtained for the d-axis control.

In the automotive field the electric motors usually include a position sensor and since it affects the charging if there are advantages it's immediate to consider using it and then not using these kind of fixed axis controls.

2.3.4 Sinusoidal voltage control

An other control technique option is to consider the sinusoidal voltage control. It controls a sinusoidal current in the d-axis while a zero current control is acting on the q-axis similarly to the d-axis control technique of Subsection 2.3.1. This control technique has been excluded in the specific case of the available motor since it has been verified that the current derivative is very high and even with a sinusoidal voltage modulation the current presents spikes with variable amplitude but with a really different waveform than the desired sinusoidal. In the specific case this control hasn't provided any advantages.

Chapter 3

Experimental testing and model calibration

3.1 Test set up

In order to be able to carry out the experimental tests, several components are required, which will be explained in the following subsections. There are the elements that constitute the iOBC's DC/DC stage, which in Figure 3.2 are included in the Electrical components block, and other components that are required in order to make the bench tests possible, and these are those included in the Measurement and control components block. In Figure 3.1 the laboratory instrumentation used is shown (in the photo it is missing the voltage generators and the computer that are on the left outside the photo). The various components are shown more clearly in Figure 3.2, where it is possible to see how they are connected to each other and the types of connections that have been established.



Figure 3.1: Photo of the laboratory workbench

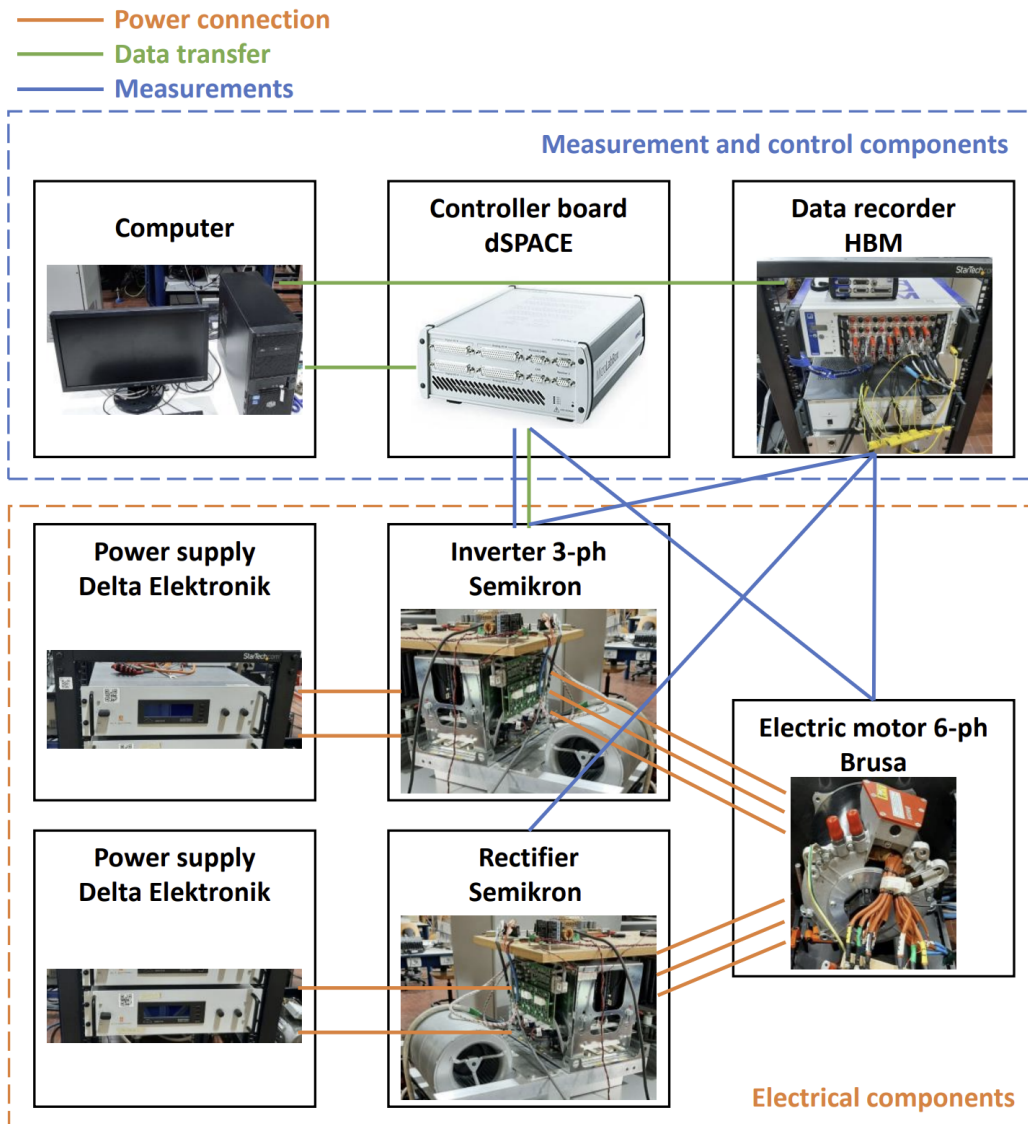


Figure 3.2: Laboratory instrumentation and interaction

3.1.1 Power components

The power components are those included within the Electrical components box in Figure 3.2 and are the following:

- The motor used for the experimental tests is a Brusa HSM1.6.17.12 motor. This is a 3-phase permanent magnet motor with a rated torque of 130Nm, base speed of 3600rpm, rated power of 70kW, designed for working with a 400V DC-link. This motor has been rewound and

adapted to 6 phases but maintaining the same number of turns. This motor has the same number of slots and topology as the FITGEN motor. The experimental flux maps of the motor in 6-phase configuration were available, and have been used in the PLECS model.

- Two 3-phase IGBT inverters are used of which one is switched off and used as a diode bridge, the model is Semikron IGDD6-1-426-D1616-E1N6-DL-FA. These are industrial inverters that allow the iOBC to be tested but do not have the same performance as automotive components in terms of switching frequencies, voltage drop and losses, and this is taken into account. They have a maximum DC-link voltage of 750V, maximum output current rms 200A, maximum switching frequency 20kHz (in experimental tests it was used 10kHz).
- For the control of the inverter it is adopted a dSpace 1202 PPC controller board that allows to quickly set up the test bench with a Simulink interface on the computer. It communicates with the inverter receiving the voltage and current information needed for the control and also the position of the rotor of the motor, and it provides to the inverter the gate signals for the IGBTs.
- In order to emulate the DC-link on the side of the AFE and the battery, two Delta Elektronik bidirectional power supply SM 500-CP-90. It can go up to 500V and to 90A, with a maximum power of 15kW.

3.1.2 Measurement instrumentation

The measurement components are those included within the "Measurement and control components" box in Figure 3.2 and are as follows:

- An high resolution data recorder Genesis GEN7i from HBM is employed to measure all the electrical signals needed. The voltages and currents are measured in both dc-links and both 3-ph sets of the electric motor and the rotor position. All the measurements are done with a resolution of 18 bit and a speed of 2 million of samples per second.
- The dSPACE used for control purposes is also used to provide the angle information.

3.2 Measurement of the leakage inductance

In order to measure the motor's leakage inductance, experimental tests were carried out using an impedance analyser, a special instrument for measuring

inductance. The electric motor circuit, as can be seen in Figure 3.3 (in order to calculate the leakage inductance, the phase resistances are not considered), contains the leakage inductances of the primary and secondary phases and the magnetising inductances. Since measurements were made on two phases at a time, the circuit is simplified as in Figure 3.4, not considering the phase that does not participate in the measurement. Moving the inductances it is possible to obtain the circuit in Figure 3.5.

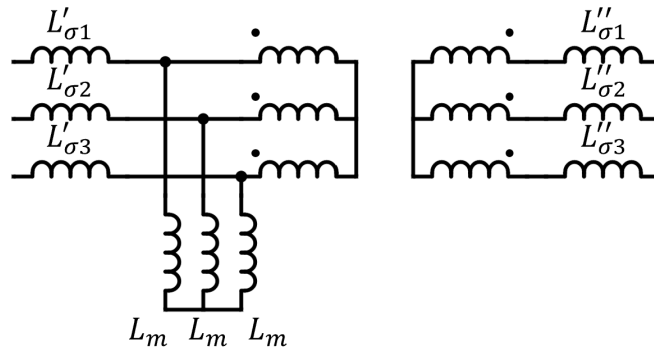


Figure 3.3: Inductances of the electric motor

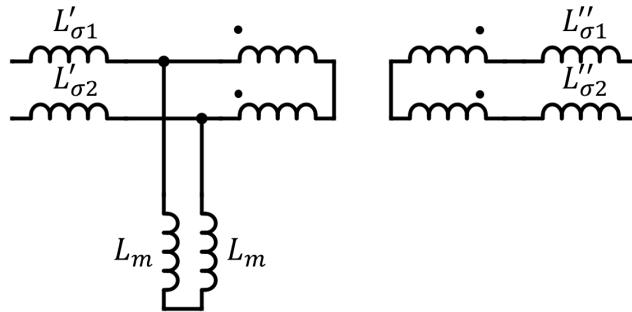


Figure 3.4: Inductances of the electric motor, circuit simplification

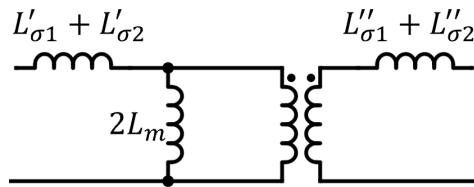


Figure 3.5: Inductances of the electric motor, circuit simplification

The measurements that can be performed on the motor, with a simplified circuit as shown in Figure 3.5, are short-circuit and open-circuit tests. The measurements made are the result of combining the leakage inductance of sets 1 and 2 and the magnetising inductance as shown in Equations 3.1, 3.2, 3.3, 3.4, obtained by considering the inductances in series and in parallel.

Since the magnetisation inductance depends on the rotor position, and since $L_m \gg L_\sigma$, it is possible and convenient to simplify the equations for calculating L_σ . $L_m \gg L_\sigma$ is verified since OC tests provide a much higher inductance than CTO tests, simplifications can therefore be made without introducing a significant error into the inductance calculation.

$$L_{OC-set1-ij} = \underbrace{(L'_{\sigma i} + L'_{\sigma j})}_{\cancel{L'_{\sigma i} + L'_{\sigma j}}} + L_m \simeq L_m \quad (3.1)$$

$$L_{OC-set2-ij} = \underbrace{(L''_{\sigma i} + L''_{\sigma j})}_{\cancel{L''_{\sigma i} + L''_{\sigma j}}} + L_m \simeq L_m \quad (3.2)$$

$$L_{CTO-set1-ij} = (L'_{\sigma i} + L'_{\sigma j}) + \frac{\underbrace{(L''_{\sigma i} + L''_{\sigma j})}_{\cancel{L''_{\sigma i} + L''_{\sigma j}}}}{\underbrace{(L''_{\sigma i} + L''_{\sigma j})}_{\cancel{L''_{\sigma i} + L''_{\sigma j}}} + L_m} \simeq (L'_{\sigma i} + L'_{\sigma j}) + (L''_{\sigma i} + L''_{\sigma j}) \quad (3.3)$$

$$L_{CTO-set2-ij} = (L''_{\sigma i} + L''_{\sigma j}) + \frac{\underbrace{(L'_{\sigma i} + L'_{\sigma j})}_{\cancel{L'_{\sigma i} + L'_{\sigma j}}}}{\underbrace{(L'_{\sigma i} + L'_{\sigma j})}_{\cancel{L'_{\sigma i} + L'_{\sigma j}}} + L_m} \simeq (L''_{\sigma i} + L''_{\sigma j}) + (L'_{\sigma i} + L'_{\sigma j}) \quad (3.4)$$

For the calculation of the average leakage inductance, the Equation 3.5 is used. The passages shown demonstrate that the average inductance between the primary and secondary is calculated with the equation of the first row.

$$\begin{aligned} L_{\sigma-mean} &= \frac{L_{CTO-set1} + L_{CTO-set2}}{8} \\ &= \frac{(L'_{\sigma} + L'_{\sigma}) + (L''_{\sigma} + L''_{\sigma}) + (L''_{\sigma} + L''_{\sigma}) + (L'_{\sigma} + L'_{\sigma})}{8} \\ &= \frac{L'_{\sigma} + L''_{\sigma}}{2} \end{aligned} \quad (3.5)$$

Table 3.1 shows the results of the measurements performed on the electric motor. While for the OC tests the measured values for all phases are reported, in the CTO tests a single value per set is reported as the measures on the different phases gave the same values.

| Test type | 3-ph set | Phases | Inductance [μH] |
|-----------|----------|--------|------------------------|
| OC | set 1 | UV | 605 |
| | | UW | 1710 |
| | | VW | 1142 |
| | set 2 | UV | 648 |
| | | UW | 1736 |
| | | VW | 1176 |
| CTO | set 1 | - | 47 |
| | set 2 | - | 48.5 |

Table 3.1: Leakage inductance measures

The leakage inductance calculated using the procedure shown and the measurements performed give an inductance of $11.9\mu H$. This value was used in the PLECS model. In addition, the leakage inductance was computed from the derivative of the current in the secondary set, measured during the experimental tests. In such way, a value of $11.6\mu H$ was evaluated, which is compatible with the leakage inductance computed in Equation 3.5.

3.3 Experimental results in alpha axis control

In order to compare the theoretical calculations concerning the waveforms shown in Section 2.1 and to carry out tests neglecting the rotor position, experimental tests are reported with hysteresis control on the alpha axis and a switching frequency of 10kHz. Differently from the Section 2.1 in this case, the d-axis of the rotor is not aligned with the alpha axis. This difference results in a variation in the values of the magnetising inductances, but still serves as a verification of the waveforms and theoretical calculations especially because the magnetising inductance was neglected in the calculation.

The waveforms of the primary voltages are shown in Figure 3.6. Since phases 2 and 3 are in parallel, the line voltages u_{12} and u_{31} are the same but with opposite sign. PWM modulation can be observed to obtain the desired value of V_h . The voltage u_{23} , on the other hand, is approximately zero due precisely to the reason that phases 2 and 3 are in parallel and because the control on the beta axis forces the current to zero and the reference is almost zero. The secondary voltages have the same trend as the primary voltages but with a voltage drop of about 20V.

Figure 3.7 and 3.8 show the primary and secondary motor currents respectively. The trend confirms the theoretical calculations with some differences. At the primary side, the magnetising current which had been neglected in the theoretical calculations is now present, and a translation of the primary current following a ramp is manifested. In addition, the phase 1 current which should be equally divided between phases 2 and 3 only flows in phase 2 as can be seen from the secondary currents. This is due to the differences in the voltage drop of the diodes which cause in this case the phase 3 not to conduct. Another difference is that more periods are spent before the current is reversed due to the delay involved in measuring the current and actuating the voltage polarity inversion of V_h . The current then exceeds the set value of I_h which in this case is 10A and approximately 30A is reached.

Figure 3.9 shows the waveforms of the power input and output of the motor. The power is pulsed due to the current trend which is also pulsed. The input power also has instants in which it is negative, and this is due to the moment in which the current reverses, resulting in the recovery of the magnetic field energy.

Figure 3.10 shows the voltage in the alpha beta reference applied by inverter 1, the one at the motor input. The instantaneous voltages that the inverter can apply are that corresponding to the vertices of the hexagon shown in Figure 2.1. During transitions between different instantaneous voltages, the voltages applied by the inverter travel through curves that are due to rapid transitions between one vertex and another of the hexagon but are of minor influence on the average values since lasts for a really short time. The moving average voltage calculated over a PWM period is then also shown in order to observe the direction and amplitude of the average voltage imposed by the inverter.

In Figure 3.11 it can be seen the primary and secondary current on the alpha beta axes. The primary current is not directed along the alpha axis but has oscillations that are due to voltage modulation. From the secondary current, it can be seen that it is tilted with respect to the alpha axis and thus to the direction in which the average voltage is applied. This is due to the cross-saturation phenomenon and the different voltage drops of the diodes which are not identical. Furthermore the current passes through phase 1 because it is excited but need to close through the other phases and the phase 2 prevails on the 3; then the secondary current is tilted -30° . The q-axis control is not able to intervene because it can act on currents that have slower variations and not on variations within the PWM period. In an attempt to reduce the q-axis current, a feed-forward control was introduced, which will be explained in the Section 4.1.2. Furthermore, the current i_3 remains zero due to the diodes in phase 3 not conducting.

Finally, Figure 3.12 shows the electrical angle of the rotor. It can be seen that the rotor is at approximately 90 degrees and thus the alpha axis is almost aligned with the -q axis. Although the current is therefore directed approximately along the q axis and thus a significant instantaneous torque is produced. The oscillations are anyway small (approximately 3 electrical degrees) because the torque produced is at high frequency and filtered by the mechanical inertia. It is important to have in mind that the test are carried out at free-shaft that is the worst case scenario since the mechanical inertia is the smallest.

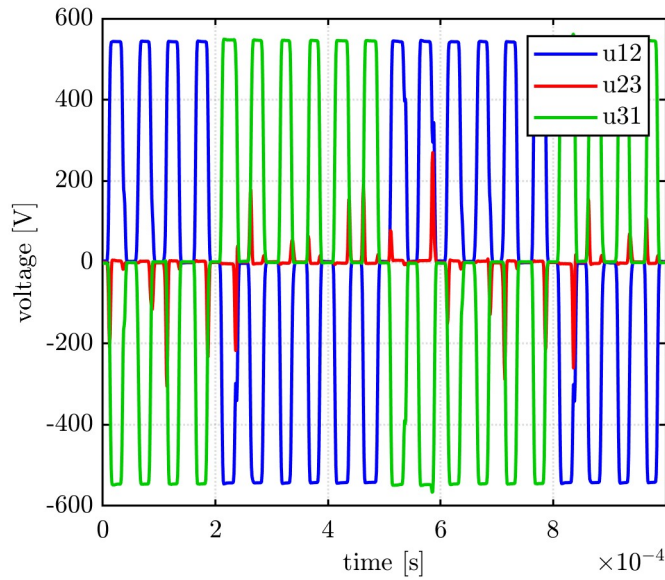


Figure 3.6: Voltage waveforms of primary side in alpha axis control at 560V in, 495V out, 200V Vh

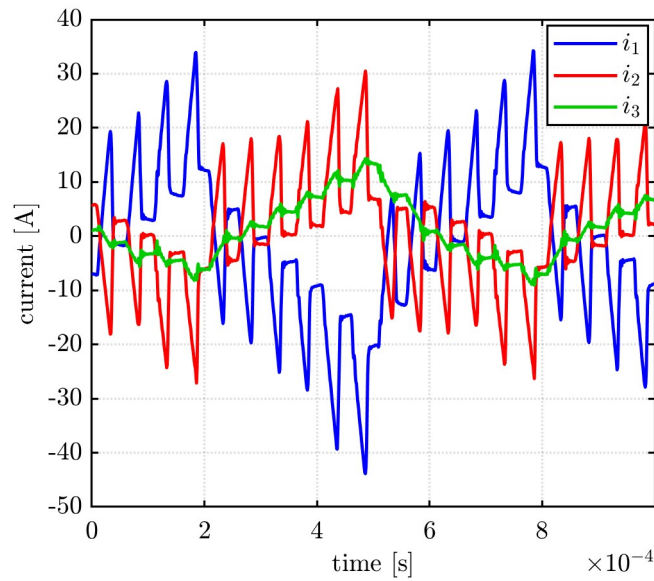


Figure 3.7: Current wave-forms of primary side in alpha axis control at 560V in, 495V out, 200V Vh

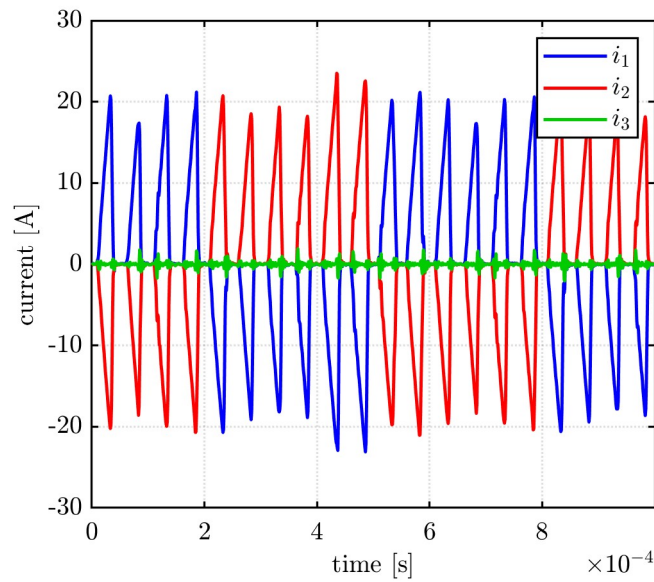


Figure 3.8: Current wave-forms of secondary side in alpha axis control at 560V in, 495V out, 200V Vh

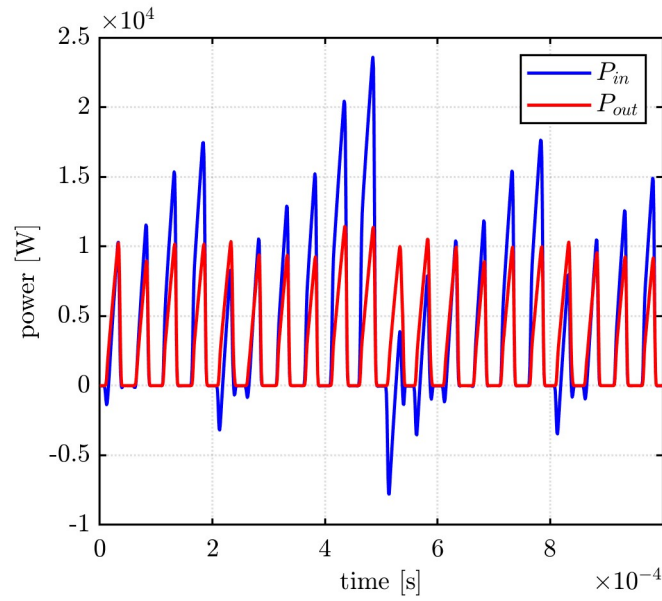


Figure 3.9: Power wave-forms in alpha axis control at 560V in, 495V out, 200V Vh

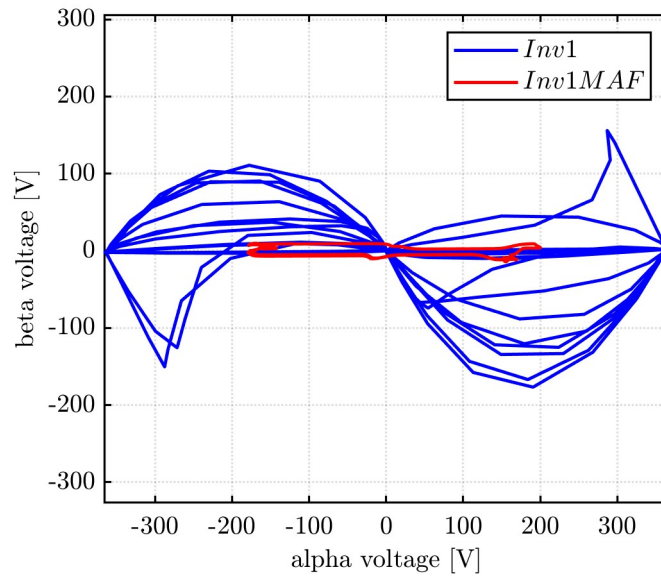


Figure 3.10: Voltage in alpha axis control in alpha-beta frame at 560V in, 495V out, 200V Vh

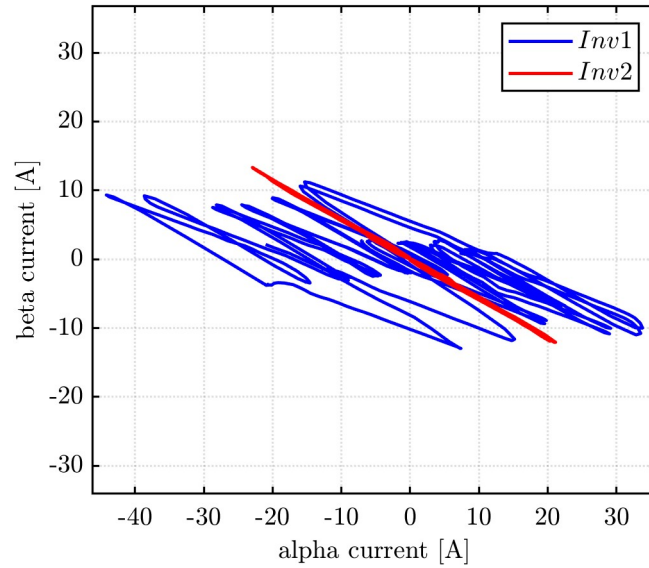


Figure 3.11: Current wave-forms in alpha axis control in alpha-beta frame at 560V in, 495V out, 200V Vh

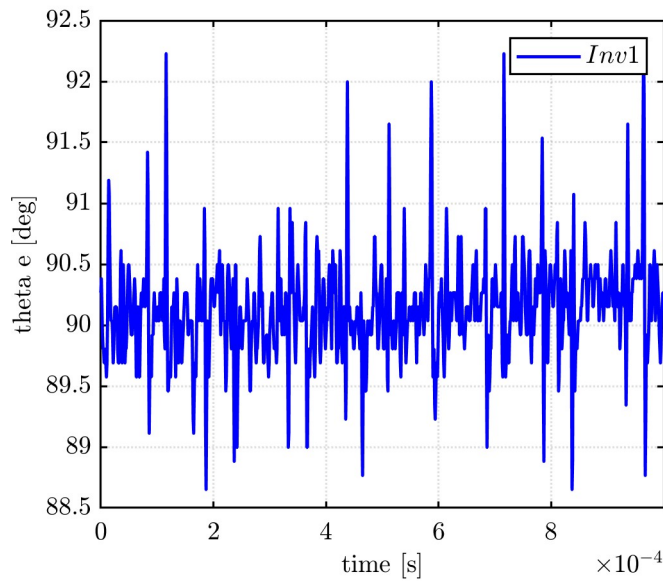


Figure 3.12: Angle in alpha axis control at 560V in, 495V out, 200V Vh

3.3.1 Sensitivity to V_h and I_h

The behaviour of the DC/DC stage in alpha-axis control when varying the control parameters V_h and I_h is studied. The aim is to better understand how they affect the charging power and efficiency directly from experimental data. Various experimental tests are therefore carried out by fixing V_h and varying I_h . In Figure 3.13 the results obtained of power input and output to the electric motor and its efficiency can be observed. Different curves can be noted at different hysteresis voltage levels as a function of the maximum primary current (maximum current module of the primary in alpha-beta axes).

The hysteresis current is varied from 5A to 90A in steps of 5A.

For the cases of $V_h = 100V$ and $150V$ the current limit was further pushed to $I_h = 110A$. For higher V_h , such high current thresholds were not possible, as the current derivative was also very high, and the measured current would considerably overcome the reference I_h . Still, because of the hysteresis control and the low phase inductance, for any reported test the measured current exceeds the imposed threshold. As an example, when $I_h = 5A$ is set, the current peaks reach 20 to 25A, depending on V_h . For this reason, the following waveforms are plotted as a function of the maximum current achieved in place of the reference I_h .

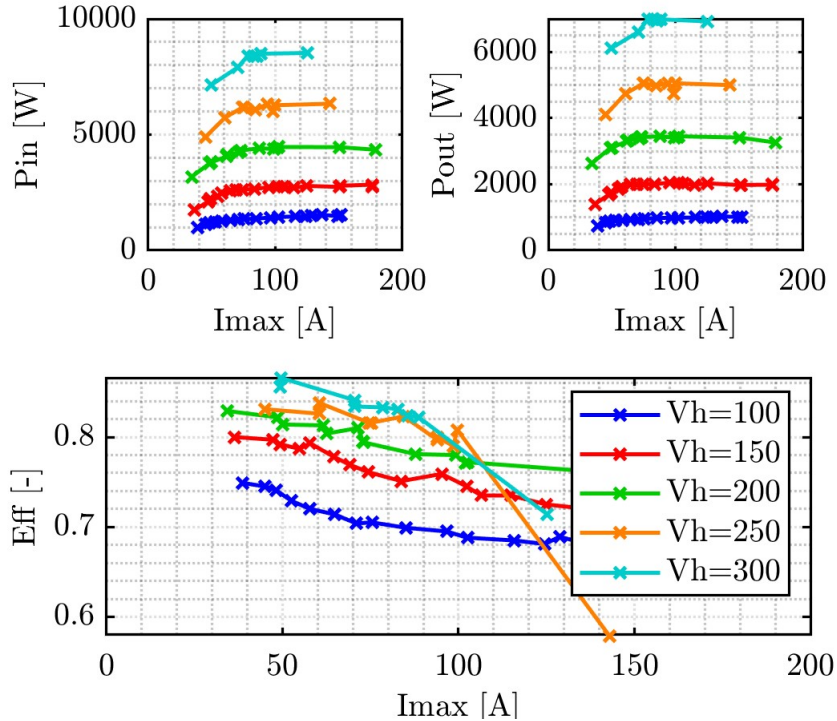


Figure 3.13: Power in input and output and efficiency at 560V in, 495V out with alpha control

In Figure 3.13 it can be observed that the power is approximately proportional to the voltage V_h . The transferred power is almost independent on the maximum current because at high maximum currents there is also a large part due to the magnetising current which does not contribute to the charging power. Observing the efficiency, it can be noted that regardless of the hysteresis voltage, it decreases as the maximum current increases. By increasing the I_h the secondary current peaks increase by a small amount and do not have a proportional increase with respect to the hysteresis current and primary current. As a result, Joule losses and iron losses increase faster than the charging power and thus the efficiency decreases. Looking instead at the efficiency as a function of V_h , it can be seen that at low values of hysteresis current (this segment is observed as the efficiency is higher) as V_h increases the efficiency also increases.

3.4 Experimental results in d axis control

The waveforms of a specific working point with d-axis control are shown in order to give an example of the waveforms that were obtained from the experimental tests. In this test, the rotor position and then the d-axis is aligned in -53.4° . Since the rotor is located close to the direction of one of the possible voltage vectors that can be supplied by the inverter, the voltage u_{31} has a low average value over a period and the current i_3 is also small (excluding the magnetising current component, which must close at this stage anyway), as can be seen from Figures 3.14, 3.15 and 3.16.

The power waveforms are shown in Figure 3.17.

Figures 3.18 and 3.19 show the voltage and current waveforms of the electric motor on the dq-axis. As with the alpha-axis control, the current is not aligned with the desired axis that in this case is the d-axis and also it is exceeded the set value of I_h which in this case is 10A.

Unlike the alpha-axis control in which the voltage vectors used among those shown in Figure 2.1 were only 2 (excluding the null vectors used to modulate the voltage amplitude), in the d-axis control the voltage vectors used are generally 4 since the direction of the d-axis does not necessarily correspond with the voltage vectors of the hexagon. The 4 voltage vectors can be seen in Figure 3.18 where the instantaneous voltage in dq axes is shown. The different phases are then used differently from the control in alpha-axis.

Excluding the difference in voltage modulation and current splitting, the explanations made in Section 3.3 concerning alpha-axis control also apply to this case of d-axis control.

Similarly to the alpha-axis control, the q axis current is forced to zero through a PI regulator. Anyway, the hysteresis frequency is in the order of 1.5 kHz, which is out of the q-axis current control bandwidth. Therefore, the PI regulator is able to control the average i_q to be zero, but it is ineffective against the HF oscillations.

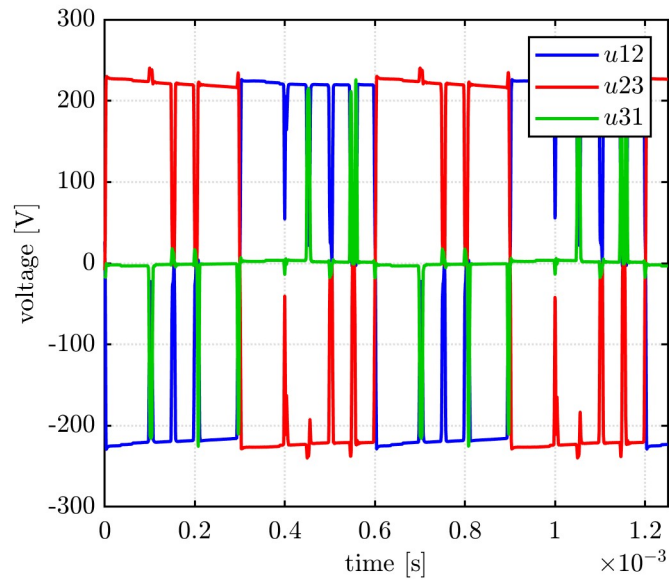


Figure 3.14: Voltage waveforms of primary side in dq control at 250V in, 200V out, 160V Vh

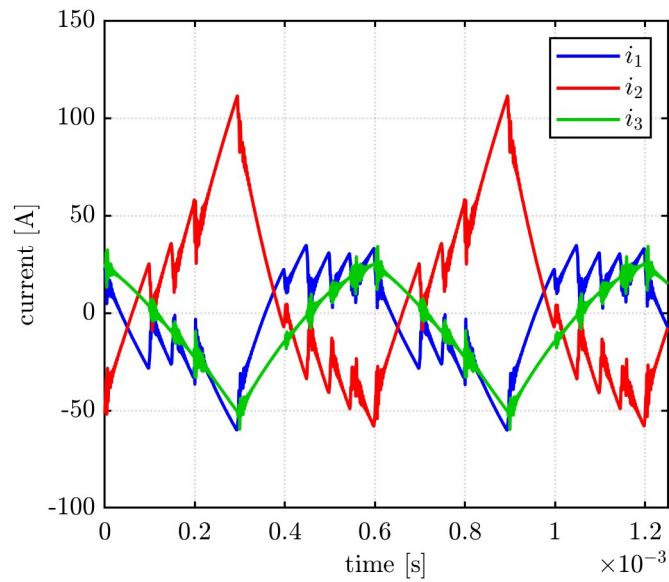


Figure 3.15: Current waveforms of primary side in dq control at 250V in, 200V out, 160V Vh

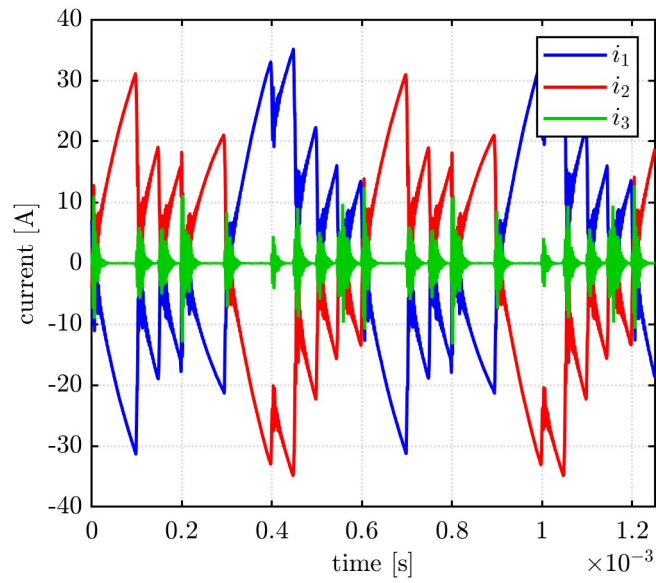


Figure 3.16: Current waveforms of secondary side in dq control at 250V in, 200V out, 160V Vh

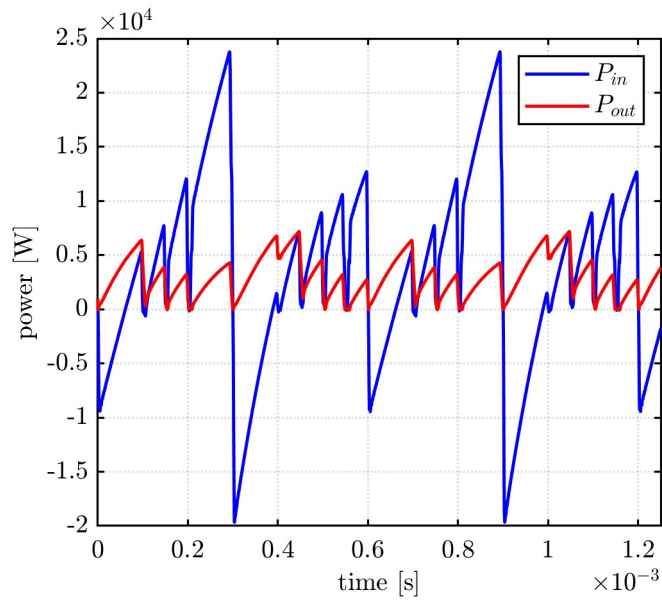


Figure 3.17: Power waveforms in dq control at 560V in, 495V out, 200V Vh

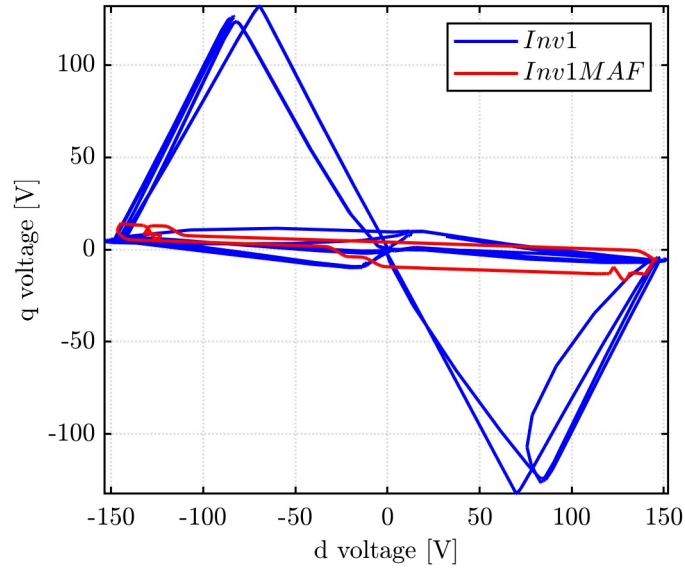


Figure 3.18: Voltage in dq frame in dq control at 560V in, 495V out, 200V Vh

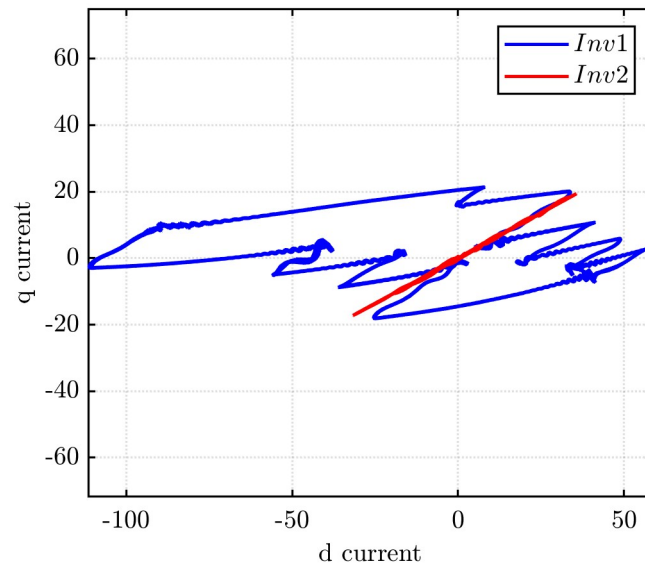


Figure 3.19: Current in dq frame in dq control at 560V in, 495V out, 200V Vh

3.4.1 Sensitivity to V_h

Experimental tests were carried out on varying the hysteresis voltage in the d-axis control. In this way, its influence on the charging power and efficiency can be observed, similar to how it is done for the alpha-axis control. In Figures 3.20, 3.21 and 3.22 respectively the power (input to the motor with a solid line and output with a dashed line), efficiency and electrical angle of the rotor can be observed. As expected, the electrical power increases with increasing hysteresis voltage. The efficiency also increases with hysteresis voltage up to about 100V and then stabilises around 77%. The electrical angle of the rotor, of these free-shaft tests, is also shown as this is a measured value and not an imposed one and influences charging. Since the rotor does not have the same position in all measurements and influences charging, fluctuations in the power and efficiency graphs are therefore observed.

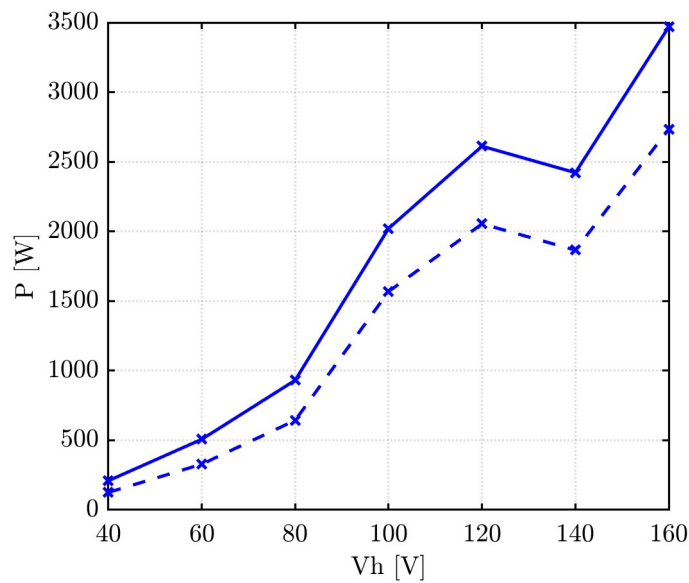


Figure 3.20: Power in input and output at 250V in, 200V out with d control

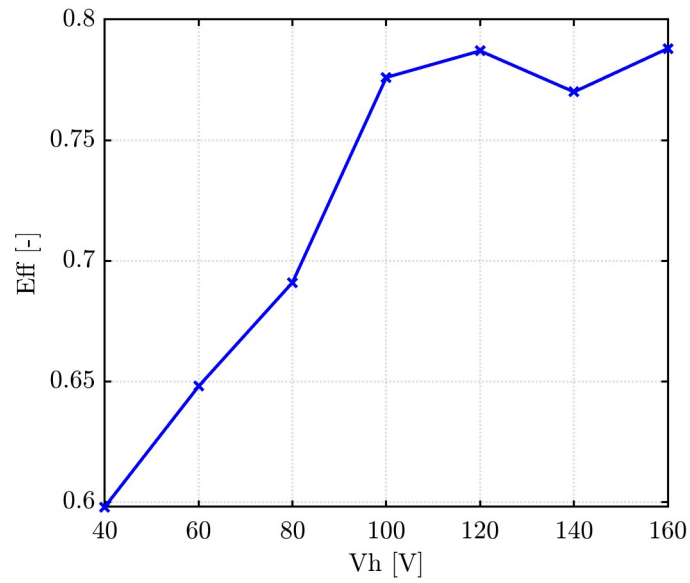


Figure 3.21: Efficiency at 250V in, 200V out with d control

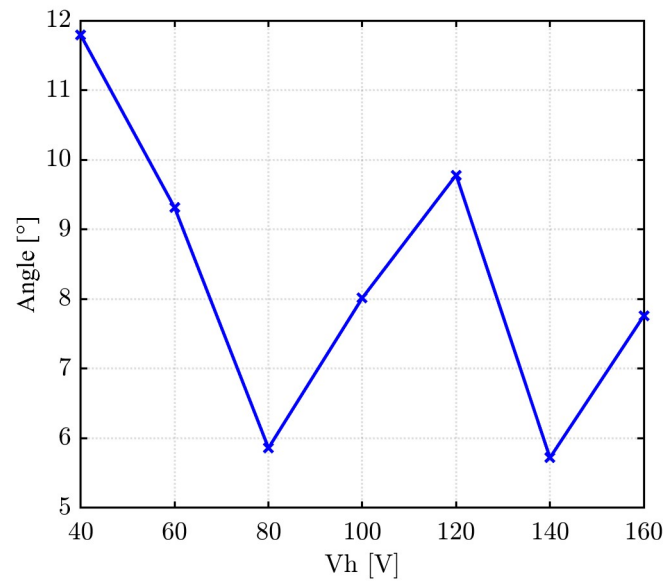


Figure 3.22: Angle in measurements at 250V in, 200V out with d control

3.5 Calibration of the PLECS model

Besides the above considerations on the charging power regulation and efficiency, the experimental test campaign was exploited to calibrate the PLECS model, in order to get a realistic representation of the charging system. It was chosen to consider an experimental test at a relatively low voltage in order to keep the iron losses low, that are not considered in the PLECS model, in order to get the experimental tests and simulations as similar as possible.

Experimental graphs and results of PLECS simulations after correcting the model are shown below. The elements that were modified to the initial model were:

- The measured leakage inductance was introduced. It affects the current derivative.
- Introduction of a delay step in the control code that represents the delay in actuation of the voltage V_h polarity that was verified experimentally.
- Corrections to the code of the hysteresis control that previously caused an asymmetric behavior.
- Modification to a block in the PLECS model of the motor. The block, shown on Figure 2.13, that caused a delay in the currents and a relevant error in the power calculation was removed.

Figures 3.23 and 3.24 compare the measured and simulated voltage waveforms. As these are imposed by the inverter unless there are errors in the model these waveforms must match.

The waveforms of the currents are shown in Figures 3.25 and 3.26. These waveforms are very similar and the result was considered adequate. The differences are due to the influence of the actual switches of both the inverter and the diode bridge, which cause also noise on the current during switching. In addition, the voltage drop of these components, as they are not all equal, causes a slightly different splitting of the currents.

From the product of the phase voltages times the currents and from the sum, the powers input and output to the electric motor are obtained and are shown in Figures 3.27 and 3.28. Since both voltages and currents are similar, the simulated and experimental instantaneous powers are also similar. The experimentally measured average powers are $P_{in} = 2179W$ and $P_{out} = 1928W$ while the powers calculated by the PLECS model are $P_{in} = 1875W$ and $P_{out} = 1750W$. Considering that the PLECS model does not include iron losses, it can be asserted that the PLECS model well represents the physical system.

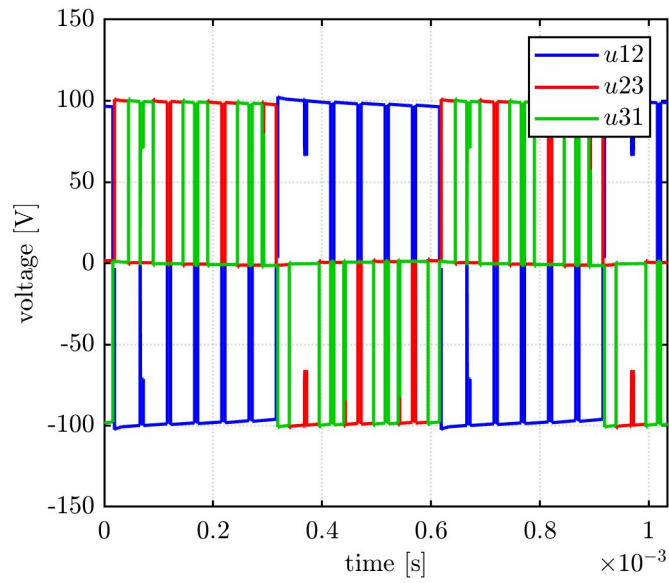


Figure 3.23: PLECS Voltage in input at 100V in, 70V out, 60V Vh

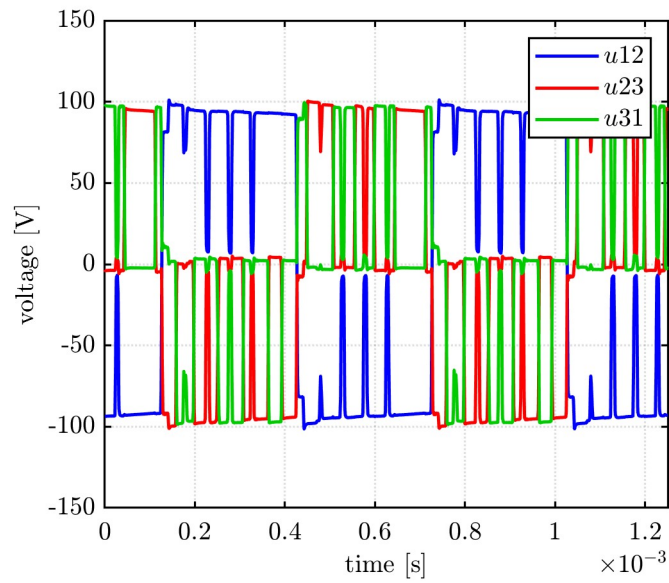


Figure 3.24: Experimental Voltage in input at 100V in, 70V out, 60V Vh

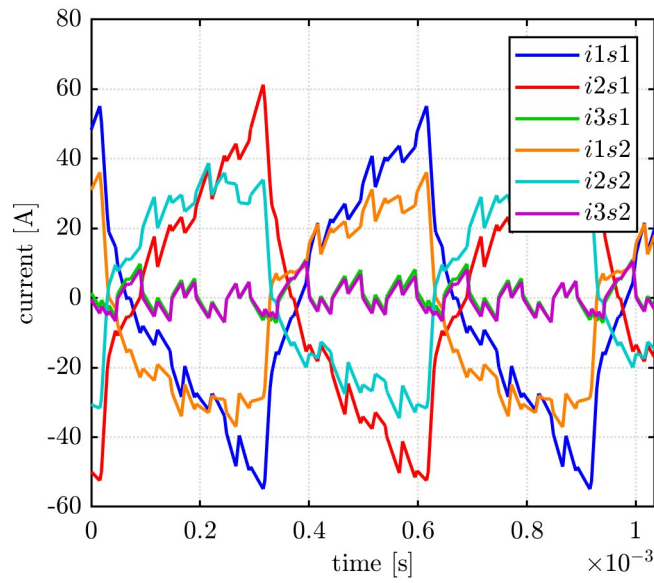


Figure 3.25: PLECS Current at 100V in, 70V out, 60V Vh

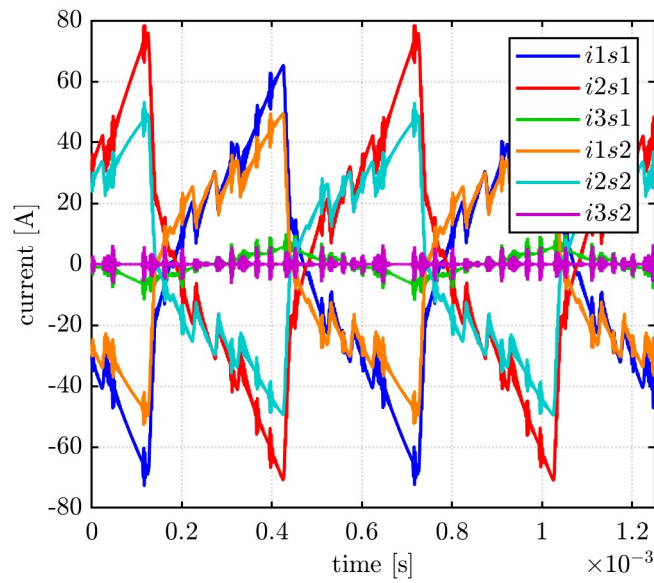


Figure 3.26: Experimental Current at 100V in, 70V out, 60V Vh

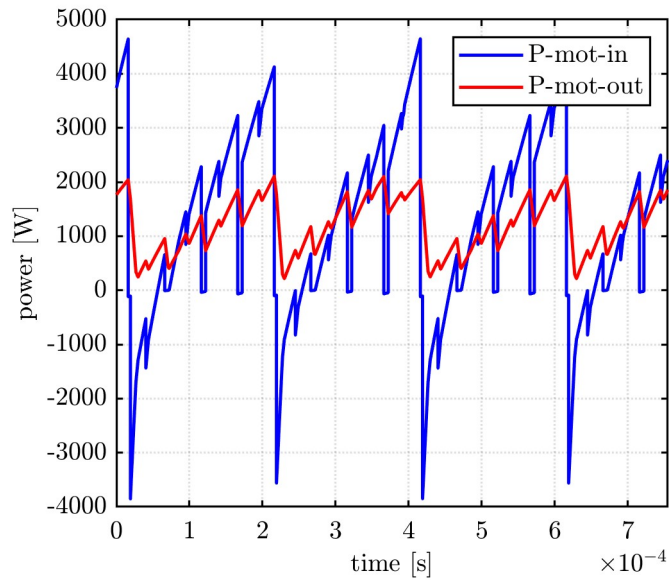


Figure 3.27: PLECS Power at 100V in, 70V out, 60V Vh

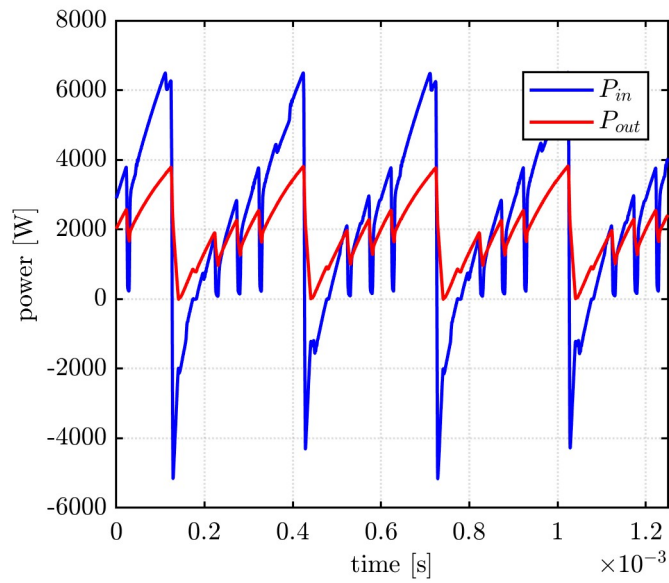


Figure 3.28: Experimental Power at 100V in, 70V out, 60V Vh

Chapter 4

Simulation Campaign

In order to investigate the operation of the converter as best as possible, a computer simulation campaign was carried out after refining the PLECS model. There are many variables affecting the charging process, and carrying out experimental tests varying all of them would have meant collecting a lot of data and it would have taken a lot of time. Instead, the model is used and numerous simulations are carried out considering all variables in an automated process.

4.1 Control refinements

Following the experimental tests carried out, by the conclusions which were obtained an attempt to improve the control was made. The problem of the d-axis current differing from the current I_h is considered and an attempt is made to reduce the q-axis current by implementing a feed forward control.

4.1.1 Maximum I_d issue not complying with I_h limit

It was noticed experimentally that the current in the d-axis largely exceeds the current limit I_h set by the control, as can be seen in Figure 3.7. Consequently, it was not possible to limit the maximum current in a specific way. It was seen that the charging power is related to the individual current peaks that are observed at the secondary side, since in most cases discontinuous operation is involved. Therefore, using high values of I_h did not prove to be productive; on the contrary, it leads to a higher magnetising current and a reduction in efficiency. Once this behaviour had been determined, it was decided to set the hysteresis current at 10A. In this way, the control reverses the polarity of the voltage V_h at the highest possible frequency. The am-

plitude of the peak current becomes a strict consequence of the hysteresis voltage V_h .

4.1.2 Feed forward on q axis

The total q-axis current considering both 3-ph sets is what determines the torque. Since the current controlled by the DC/DC stage is only the primary current, an attempt is made to act uniquely on this to minimise torque production. Due to the cross-saturation phenomenon, an undesirable q-axis current can be obtained even if no q-axis voltage is imposed. To try to minimise this, a feed-forward voltage is implemented to be given in the q-axis.

To calculate the feed-forward voltage, the assumption is made that the q-axis current is zero-controlled and therefore the terms due to the q-axis current in the following equations will be neglected. It is considered the electric equation of the stator in dq-axis shown in Equation 4.1. In Equation 4.2 the electrical equation of the q-axis separately is shown.

$$v_{dq} = Ri_{dq} + \frac{d\lambda_{dq}}{dt} + j\omega\lambda_{dq} \quad (4.1)$$

$$v_q = Ri_q + \frac{d\lambda_q}{dt} + \omega\lambda_q \quad (4.2)$$

Are considered the magnetic Equation 4.3 of the d-axis and the derivative of the magnetic Equation 4.4 of the q-axis.

$$\lambda_d = L_d i_d + \cancel{L_{dq} i_q} \quad (4.3)$$

$$\frac{d\lambda_q}{dt} = l_{dq} \frac{di_d}{dt} + \cancel{l_q \frac{di_q}{dt}} \quad (4.4)$$

In the Equation 4.2 are substituted the Equations 4.3 and 4.4. It is obtained the Equation 4.5.

$$v_q = \cancel{Ri_q} + l_{dq} \frac{di_d}{dt} + \omega \cancel{L_d i_d} \quad (4.5)$$

Simplifying the equation 4.5 by considering that the current in the q-axis is zero and the rotor is stationary, it is obtained the Equation 4.6.

$$v_q = l_{dq} \frac{di_d}{dt} \quad (4.6)$$

Following the same procedure as for the q-axis also on the d-axis is obtained an equation analogous to the Equation 4.6 but referring to the d-axis

in which the differential inductance in the d-axis appears and not the crossed inductance. Considering the approximation of the current derivative on the d-axis in which the instantaneous voltage is substituted for the mean voltage imposed on the d-axis as in Equation 4.7, from Equation 4.6 it is obtained the Equation 4.8.

$$\frac{di_d}{dt} = \frac{V_{hyst}}{l_d} \quad (4.7)$$

$$v_q = \frac{l_{dq}}{l_d} V_{hyst} \quad (4.8)$$

Equation 4.8 therefore makes it possible to calculate the voltage to be imposed on the q-axis in order to keep the q current to zero.

The calculated feed-forward voltage is based on the instantaneously measured values of current and inductance. Since the current in a period varies greatly due to the high current derivative, the feed-forward compensation is not exact because the differential inductance values also vary. However, an attempt is made by means of this compensation to reduce the current in the q-axis.

From the results of the simulations, the implementation of feed-forward control did not produce any useful results. In steady state, a small increase in q-axis current and torque was obtained. The only situation in which it brought some benefit was during transients in which the mean square current in the q-axis was reduced and also the torque, but by a few percentage points.

In the experimental data, moreover, the torsion of the current with respect to the q-axis is not so much due to the cross-saturation phenomenon but more to the different conductivity of the diodes.

The feed-forward control was then implemented in the control routine but not subsequently used to carry out the rest of the simulations.

4.2 Parametric Analysis

4.2.1 Automation

In order to map the operation of the DC/DC stage of the iOBC, it is necessary to carry out numerous simulations as the parameters of interest change. The parameters considered are the following: hysteresis voltage, hysteresis current, input voltage, output/battery voltage, rotor angle.

There are many simulations to be carried out, and it is therefore necessary to automate the process by which simulations are run and data is saved and processed. The scheme of Figure 4.1 shows the procedure employed to automate the process.

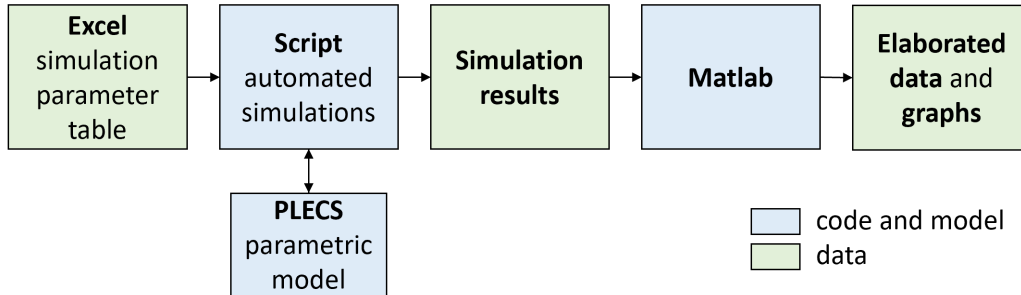


Figure 4.1: Parametric analysis procedure

A PLECS model was created in which the parameters to be varied in the different simulations are written as variables. A PLECS Script makes it possible to update these variables automatically via a for loop, run simulations and export the desired data. The Script automatically starts subsequent simulations with the desired parameters previously saved in tables. When the waveforms reach a steady state operation, the data in a preset time interval are saved. Data of interest including voltages, currents and powers at various points on the OBC are saved. The data is imported into Matlab and considering the hysteresis voltage variation, which is a square wave, are identified the time periods over which the average values of the powers are calculated. It is then possible to save the powers and efficiency at all working points on which simulations are conducted. After saving the results of several simulations, it is possible to map the powers and efficiency depending on the desired parameters.

4.2.2 Sensitivity to V_h and I_h

As a first analysis, the control parameters V_h and I_h are varied. An input voltage of 550V and a battery voltage of 400V are considered as plausible voltage values for an OBC. The trends expected from the initial theoretical calculations and experimental tests are confirmed. In Figures 4.2 and 4.3 the maximum power and current in the d-axis increase as V_h increases. The efficiency, shown in Figure 4.4, also tends to increase as the hysteresis voltage increases. As explained earlier, the hysteresis current value that provides the best efficiency is the lowest.

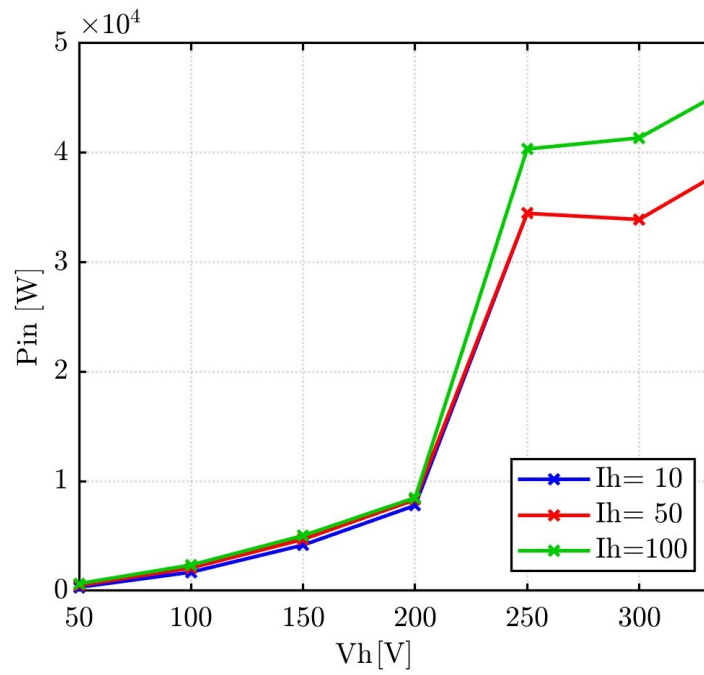


Figure 4.2: V_h and I_h influence at 400V out, 550V in with d control

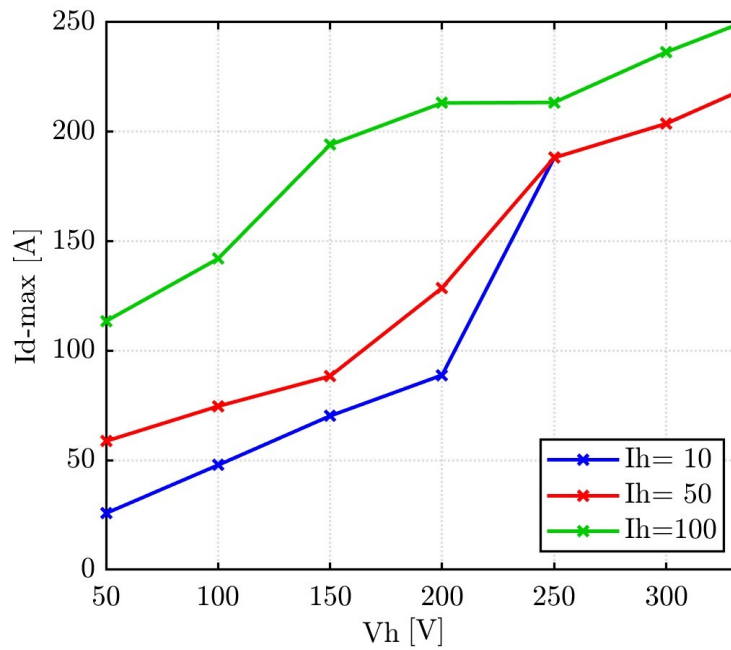


Figure 4.3: V_h and I_h influence at 400V out, 550V in with d control

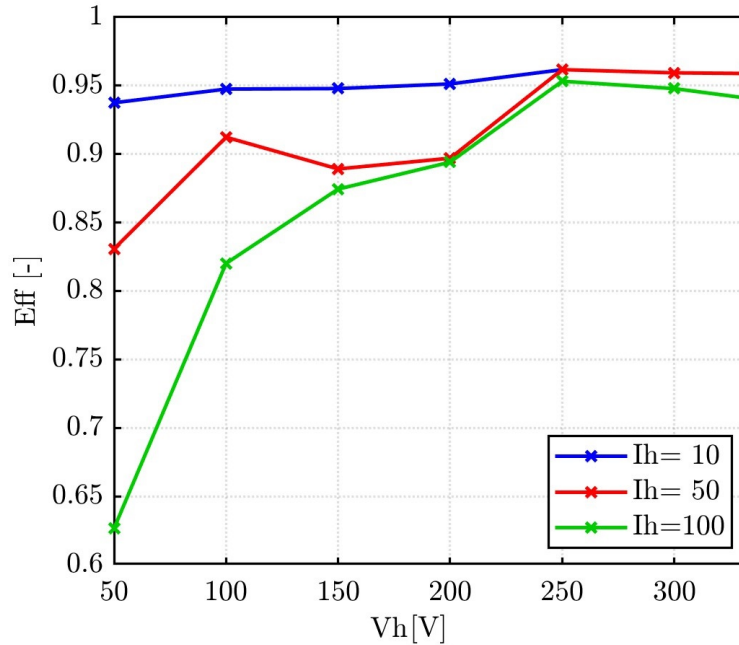


Figure 4.4: V_h and I_h influence at 400V out, 550V in with d control

4.2.3 Angle influence on charging

In order to study the influence of angle on charging power, simulations are carried out in which the only parameter that is varied is the position of the rotor. It is varied between 0 and 60 electrical degrees in steps of 5 degrees. Considering that the possible instantaneous voltages are those of the hexagon in Figure 2.1, there is a periodicity of 60 degrees in which given the symmetry, already between 0 and 30 degrees every possible case can be studied. The assumed symmetry is confirmed in Figure 4.5. By varying the position of the d-axis and thus the direction in which the voltage V_h is supplied, each phase can be more or less utilised in the sense that the voltage supplied to it is changed and also the current flowing through it. Depending on whether all three phases are utilised or one is excluded because it is, for example, orthogonal to the voltage vector, the equivalent leakage inductance (as can be seen in Figure 2.3) that could be calculated is not constant. The derivative of the current depends on the leakage inductance as shown in Equation 2.1. This then results in a variation of the maximum current in the d-axis and the power as the rotor position varies. In addition, the current divides differently in the three phases causing variation in the overall Joule losses of the electric motor.

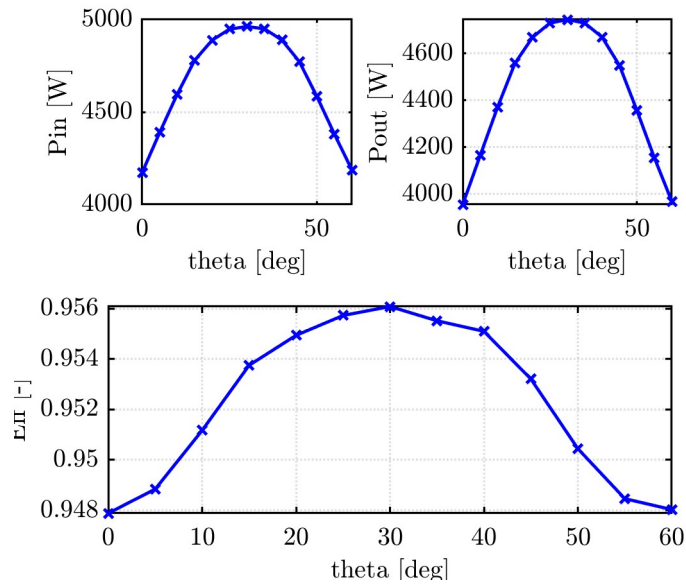


Figure 4.5: Angle influence at 550V in, 400V out, 150V Vh with d control

4.2.4 Sensitivity to Vdc1 and Vh

From the previous sections, it was decided to set the hysteresis current value at 10A. The remaining parameters on which it is possible to act in order to control charging are therefore the hysteresis voltage and the dc-link voltage at the input to the DC/DC stage. Figures 4.6, 4.7 and 4.8 in which the input power (represented with a solid line) and output power (represented with a dashed line), the efficiency and the maximum current in the d-axis are shown respectively.

In Figure 4.6 it can be seen that the power increases as the hysteresis voltage increases but also as the input voltage, called V_1 , increases. At the same voltage V_h , the average voltage supplied by the inverter in the d-axis is the same but the current depends on the difference between the input and output voltages, which is the voltage applied to the leakage inductance. Equation 4.9, obtained by considering the control in alpha-axis and the simplified circuit in Figure 2.3, allows to show analytically that as the input voltage increases, the maximum current increases with a consequent increase in the charging power.

$$\begin{aligned}
 \Delta i &= \frac{(V_1 - V_2)dT_{sw}}{3L_\sigma} = \frac{(\frac{2}{3}\frac{V_h}{d} - V_2)dT_{sw}}{3L_\sigma} \\
 &= \frac{(\frac{2}{3}V_h - V_2d)T_{sw}}{3L_\sigma} = \frac{2}{3}V_h \frac{(1 - V_2/V_1)T_{sw}}{3L_\sigma}
 \end{aligned} \tag{4.9}$$

This behavior was verified in simulation as shown on Figure 4.8.

With regard to efficiency, it can be seen in Figure 4.7 that there is also a dependence on the input voltage. It seems to be convenient to keep V_1 voltage as high as possible when working at low V_h , while at high V_h of the curves shown the one at 500V is the optimum. It would be better to observe the efficiency in relation to power. It can be seen that at powers below 4kW, the voltage V_h drops below 200V as soon as V_1 is increased over 460V in order to obtain a better efficiency. Therefore V_h stands in the range where a higher V_1 voltage seems convenient. In this graph, however, iron losses are not taken into account, which will be considered later and which strongly affect efficiency.

In Figure 4.8 the maximum currents in the d-axis are shown having set the I_h at 10A, the issue that the I_h is exceeded by a large margin still appears.

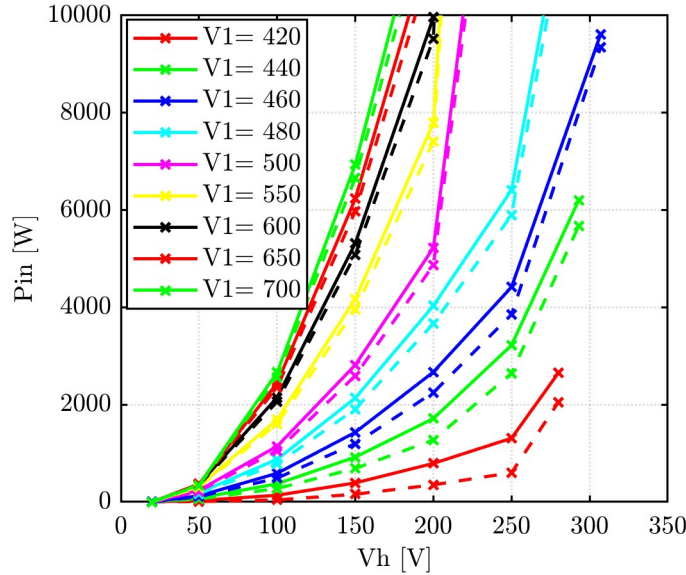


Figure 4.6: V_h and V_1 influence at 400V out with d control

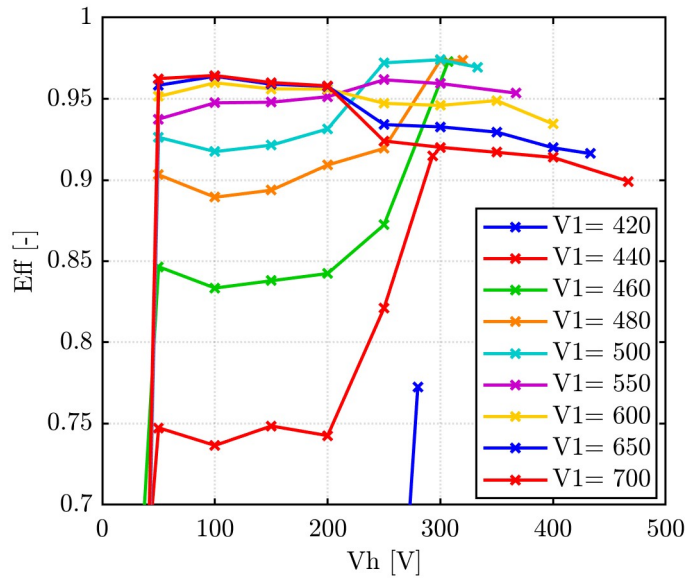


Figure 4.7: Vh and V1 influence at 400V out with d control

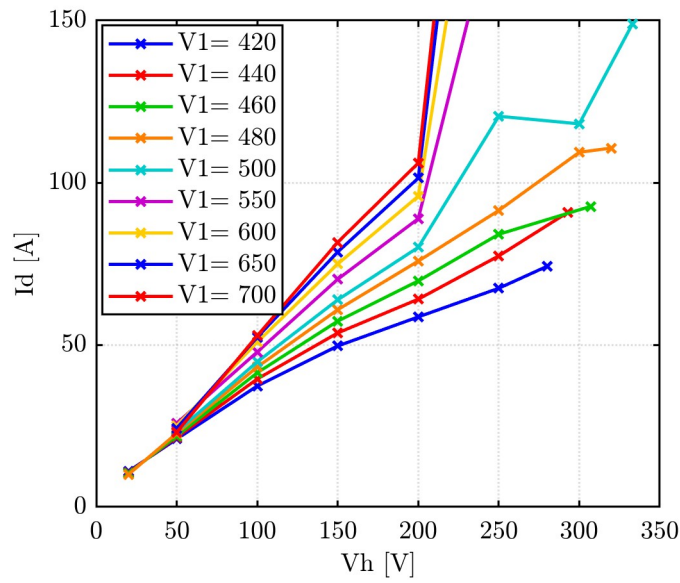


Figure 4.8: Vh and V1 influence at 400V out with d control

4.3 New proposed CC control technique

4.3.1 Description of the Control Technique

The DC/DC stage of the converter defines the battery charging power while the AFE has the function of keeping the dc-link voltage stable (voltage at the input of the DC/DC stage). In order to regulate the power a control loop must be introduced for the DC/DC stage. Through the control parameters of the DC/DC stage there is the need to control the desired charging power with acceptable dynamics and stability. In order to control the charging power a battery current reference can be produced by dividing the desired charging power by the battery voltage. Otherwise, the charging current can be adjusted by generating a current reference as a standard OBC scheme. This second case is what is used and illustrated in Figure 4.9. Through a PI controller that has the battery voltage error as input it is produced as output the reference current that is saturated to meet the current limits.

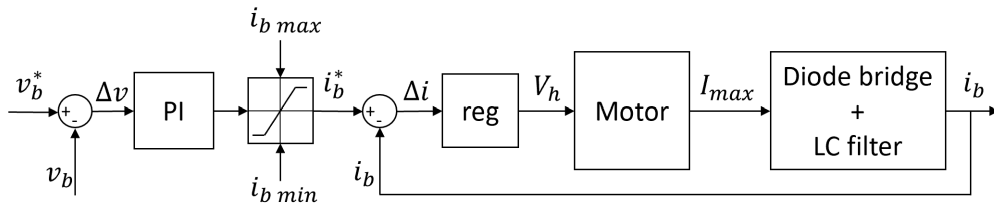


Figure 4.9: Battery charging current control loop

The hysteresis current I_h is kept at 10A for the reasons explained earlier and to have a higher efficiency, for this reasons it does not appear in the control scheme. Assuming the input dc-link voltage fixed by the AFE (it can be regulated in order to meet the best efficiency for example considering a LUT), the way that has been found to adjust the charging current is to act on the hysteresis voltage V_h . As shown on Figure 4.9, from the error of the reference current, the hysteresis voltage command is generated through a controller. The maximum current reached in the d-axis is related to the magnitude of the hysteresis voltage as explained in Section 4.2.4 and as can be seen in Figure 4.8. Through the diode bridge (that rectifies the output current from the motor) and through the LC filter placed before the battery, the battery charging current is obtained.

The Subsection 4.3.2 explains how the "Motor" and "Diode bridge + LC filter" blocks in Figure 4.9 were implemented. In addition, the Subsection 4.3.2 shows how the current control loop was sized while the Subsection 4.3.3 shows the simulation results.

4.3.2 Control calibration

For the calibration of the current control loop there is the need to know the dynamic behavior of the DC/DC stage and the related components. From the DC/DC stage point of view, since the leakage inductance is small and the current derivative is high, the desired power can be set in just some PWM time periods, the ones needed for the current to reach the maximum limit I_h . This behavior could be considered as a low pass filter with a time constant equal to the time that the d axes current requires to reach its maximum. Assuming that the maximum current exceeds current I_h in a single period, the maximum current in d-axis can be calculated as in Equation 4.10. Equation 4.10 is obtained simply from Equation 2.1 of the inductor by considering the alpha-axis equivalent circuit shown in Figure 2.3 and multiplying by the transfer function of the low-pass filter.

$$I_{max} = \frac{dV_1 T_{sw}}{3L_\sigma} \frac{1}{1 + sT_{sw}} = \frac{V_h T_{sw}}{2L_\sigma} \frac{1}{1 + sT_{sw}} \quad (4.10)$$

For the calculation of the current to the battery instead there is the need to consider also the battery side LC filter. It has a second order transfer function that is shown in Equation 4.11.

$$\frac{i_b}{i_{out}} = \frac{1}{1 + s^2 LC} \quad (4.11)$$

In Equation 4.11 the current coming from the diode bridge is called i_{out} .

The cut frequency of the LC filter is calculated in Equation 4.12.

$$\omega_c = \frac{1}{\sqrt{LC}} = \frac{1}{\sqrt{30 * 10^{-6} H * 7 * 10^{-3} F}} = 2182 \frac{rad}{s} \quad (4.12)$$

To relate the battery current with the maximum value of i_{out} , that is also the maximum value of the current on the d-axis, it is considered the steady state power balance and it's obtained the Equation 4.13 that is calculated starting from the Equation 2.4.

$$i_b = \frac{P}{V_b} = \frac{1}{2} I_{max} \frac{dV_1}{V_b} = \frac{1}{2} I_{max} \frac{3 V_h}{2 V_b} \quad (4.13)$$

In order to avoid the influence of V_h on the battery current it's considered that dV_1/V_b is near 1 and then neglected. This simplification leads to some further errors on the bandwidth calculation at low duty cycles but it's not critical, as proven by simulation results. Another reason why this simplification is used is that high V_h allows to have higher efficiencies and then are preferred (even if obviously it is set depending also on the power needed). Otherwise could

be considered a non constant gain in the control loop as can be employed in the control of a standard AFE.

Another filter, equal to the battery side one, is put between the AFE and the DC/DC stage. Since the capacitor and inductor employed to build both filters are the same, also the cut frequency is the same.

Considering the time response evaluated and introducing a pure integral regulator, it's obtained the control loop of Figure 4.10.

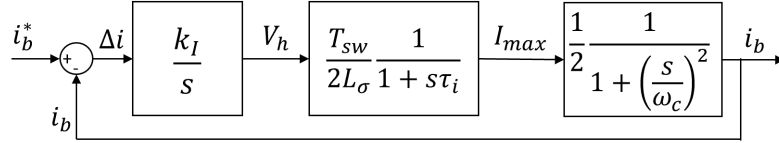


Figure 4.10: Battery charging current control loop

The power control regulator chosen is a pure integral regulator. Since there is not the need to cancel a pole of the transfer function, the proportional regulator is not comprehended. The power control loop shouldn't interact with the AFE voltage control neither with the LC filters at the sides of the DC/DC stage. For this reason the bandwidth of the power control should be one decade lower than the AFE one and also a decade lower than the cut frequency of the LC filter. After these considerations, the control loop of Figure 4.10 can be simplified neglecting the low pass filter $1/(1 + s\tau_i)$ and the LC transfer function dynamics instead just considering their steady state equations.

In order to calculate the time response of the system it's calculated the closed loop transfer function, starting from the open loop one shown in Equation 4.14.

The transfer function in open loop becomes as shown in Equation 4.14.

$$H_{OL} = \frac{k_i T_{sw}}{s} \frac{1}{2L_\sigma} \quad (4.14)$$

The transfer function in closed loop is calculated in Equation 4.15.

$$H_{CL} = \frac{H_{OL}}{1 + H_{OL}} = \frac{k_i \frac{T_{sw}}{4L_\sigma}}{s + k_i \frac{T_{sw}}{4L_\sigma}} = \frac{1}{s \frac{4L_\sigma}{k_i T_{sw}} + 1} \quad (4.15)$$

The bandwidth is then calculated as in Equation 4.16.

$$\omega_b = \frac{k_i T_{sw}}{4L_\sigma} \quad (4.16)$$

Then known the desired bandwidth, the integral gain is calculated as in Equation 4.17.

$$k_i = \omega_b \frac{4L_\sigma}{T_{sw}} \quad (4.17)$$

Considering a bandwidth of $\omega_b = 218rad/s$ corresponding to 10 times slower than the cut frequency of the LC filter shown in Equation 4.12, the leakage inductance calculated on section 3.2, a switching frequency of $10kHz$, it's calculated a $k_i = 104$. The time constant can be calculated as in Equation 4.18.

$$\tau = 2\pi/\omega_b = 29ms \quad (4.18)$$

4.3.3 Simulation Results

The type of control explained was implemented in the PLECS model. The input of battery current measurement was added to the "Motor control" block in Figure 2.7. The C code with a pure integral controller for the battery current and the calculated gain was implemented to have the desired bandwidth of $29ms$.

Several simulations were carried out, all with a battery voltage of $400V$ and a battery reference current of $15A$, varying the input dc-link voltage from $400V$ to $700V$ at $50V$ intervals. At the beginning of the simulation, the battery current and hysteresis voltage are set to zero so that the simulations correspond to step responses. In Figures 4.11 and 4.12 it can be observed respectively the control signal V_h generated by the integral control and the system response by observing the battery current.

Depending on the primary voltage the time response is slightly different but in any case the band is close to the desired one. There is current ripple even at steady state that do not depend on the realized battery current control but on the current discontinuity that cancels with each PWM period. To reduce the battery current ripple, it is necessary to act on the battery-side LC filter. In the curve with input voltage of $450V$, it can be noticed that the hysteresis voltage saturates and the reference current cannot be reached because the input voltage is too low.

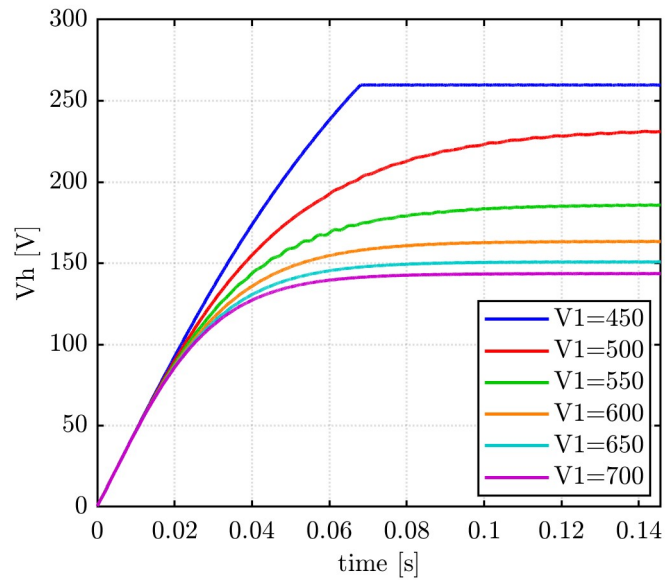


Figure 4.11: Battery current control at 400V battery voltage

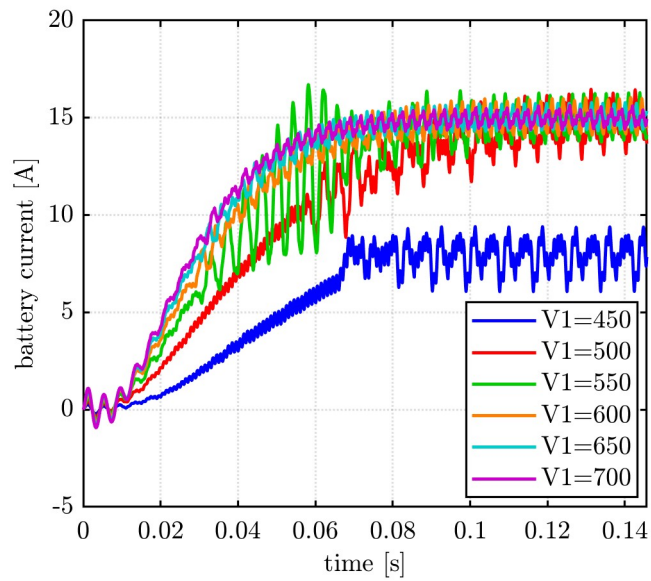


Figure 4.12: Battery current control at 400V battery voltage

4.3.4 Constant Voltage Results

In addition to developing the control code needed to adjust the battery current and fix it to a desired value, the CV control was implemented. It consists of the left part of Figure 4.9.

In order to test both CC and CV control, the battery need to be modeled in a way that while charging it increases its voltage. Then it is modeled with a capacitor and resistor calculated so that the battery with a current of 15A is charged from 400V to 450V in 0.7s and so that the internal resistance of the battery has a voltage drop of 5V when there are 15A.

For the voltage control it is considered a purely proportional regulator. The proportional gain is calculated in order to have a bandwidth 10 times slower than the battery current regulator one to avoid interaction between the internal and the external control loops. The battery current limits are set to -15A and 15A. A simulation is conducted with input dc-link voltage at 600V and an initial battery voltage of 400V. The measured battery current and voltage are shown in Figure 4.13.

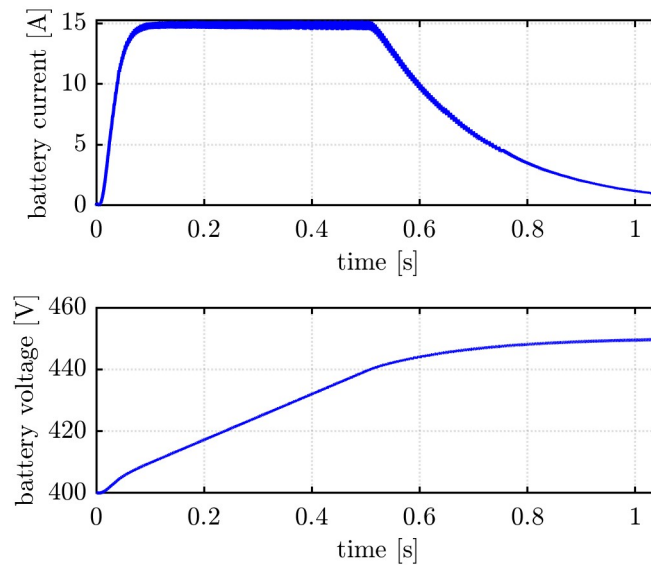


Figure 4.13: Battery current control CC and CV

As can be seen in Figure 4.13, the battery current has an initial steep slope. It is due to the inner control loop that adjusts the current with a reference of 15A, a value coming from the outer loop. The outer loop would provide an higher current reference but it is saturated. In order to reach the value of 15A the inner loop(which can be seen in Figure 4.9) sets the hysteresis

voltage value which also has an initial steep slope and then stabilizes. By receiving constant charging current, the battery recharges following a ramp. The hysteresis voltage also keeps increasing slowly to maintain the desired current.

When the battery voltage approaches its reference value of 450V the CV control intervenes and begins to reduce the charging current that reaches zero when the battery is fully charged.

4.4 Iron losses of the electrical machine

In order to make the results of the PLECS model more complete, it was decided to take into account the iron losses of the electric motor, which until now have not been considered in the model. Using experimental measurements, the iron losses are calculated as the difference between the average power input and output to the electric motor and subtracting the average Joule losses. Equation 4.19 is then considered to calculate the iron losses, where the Joule losses are calculated as in Equation 4.20.

$$P_{Fe} = P_{in} - P_{out} - P_{Cu} \quad (4.19)$$

$$P_{Cu}(t) = R_{Cu} \sum_j [\dot{i}_j(t)]^2 + [\ddot{i}_j(t)]^2 \quad (4.20)$$

Joule losses depend on resistance, which in the other hand depends on temperature. During experimental tests it was estimated that the maximum temperature variation was from 20° to 60°. Considering the temperature coefficient of copper the resistance varied by 17%. However, considering that the experimental results show that the iron losses are generally an order of magnitude higher than the Joule losses in the charging configuration, the influence of temperature is neglected.

The values of iron losses obtained in this way will be used to adjust the performance and power calculated by the PLECS model. Using the Equation 4.21, iron losses are added to the input power, in the same way as PLECS acts in considering switch losses.

$$\eta = \frac{P_{out}}{P_{in} + P_{Fe}} = \frac{P_{out}}{P_{in}} \frac{P_{in}}{P_{in} + P_{Fe}} = \eta_{PLECS} \frac{P_{in}}{P_{in} + P_{Fe}} \quad (4.21)$$

In order to map the losses and be able to calculate them at each operating point, it is necessary to know what they depend on. Therefore, the Equations 4.22 and 4.23 are observed, which allow the theoretical calculation respectively of hysteresis losses and iron losses per unit volume. Once

the material composing the electric motor has been determined, it can be noted that both types of losses depend uniquely on magnetic induction and its frequency.

$$p_{Fe-hyst} = k_{hyst} B_{max}^y f [W/kg] \quad (4.22)$$

Where the coefficient y depends on the material and can vary between 1.6 and 2.

$$p_{Fe-ec} = k_{ec} B_{max}^2 f^2 \delta^2 [W/kg] \quad (4.23)$$

On Equation 4.23 ed stands for eddy currents. δ is the thickness of the iron layers.

It is therefore necessary to relate the experimentally measurable quantities to the magnetic induction and its frequency. The parameters that have been considered determining are the maximum magnetising current because proportional to the magnetic induction and its frequency. In the experimental data the current ripple due to PWM modulation is present, it depends on the voltages at the ends of the DC/DC stage and the duty cycle. Although this factor affects iron losses, it is not taken into account as it is considered to be of secondary importance compared to the other parameters considered.

The experimental data taken into account to create the iron loss map are shown in Figure 4.14 and represented by blue dots. In order to recalculate the losses at other points, a third-order fit is considered for both magnetising current and frequency as it was found to approximate the data reasonably well. In addition, in order to obtain meaningful trends when approaching the axes, data points were added with iron losses imposed equal to zero on the axes at zero frequency and zero current.

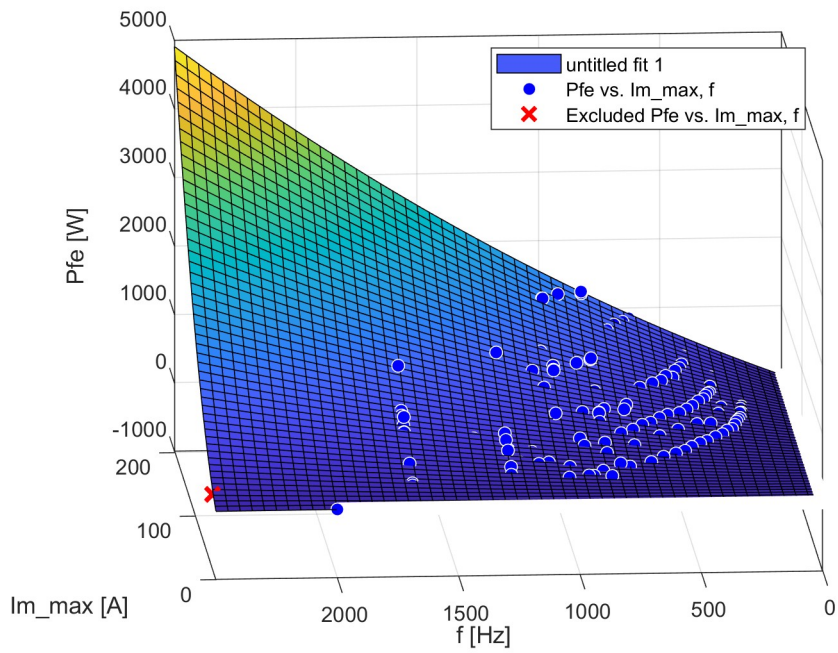


Figure 4.14: Iron losses 3D plot

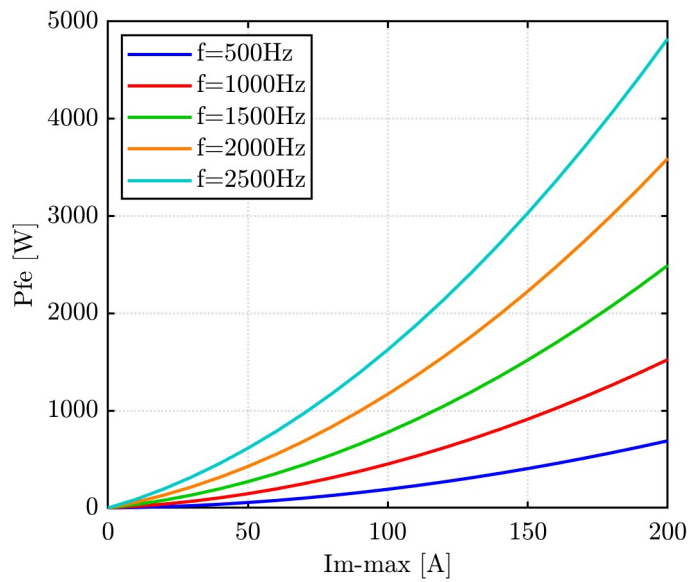


Figure 4.15: Iron losses 2D plot

Figure 4.15 shows some of the constant-frequency curves that lays on the plane interpolating the measured iron loss data.

Considering the data from the same simulations used to make the graph in Figure 4.7 and adding the iron losses to the input power in the way explained, the efficiency curves shown in Figure 4.16 were obtained.

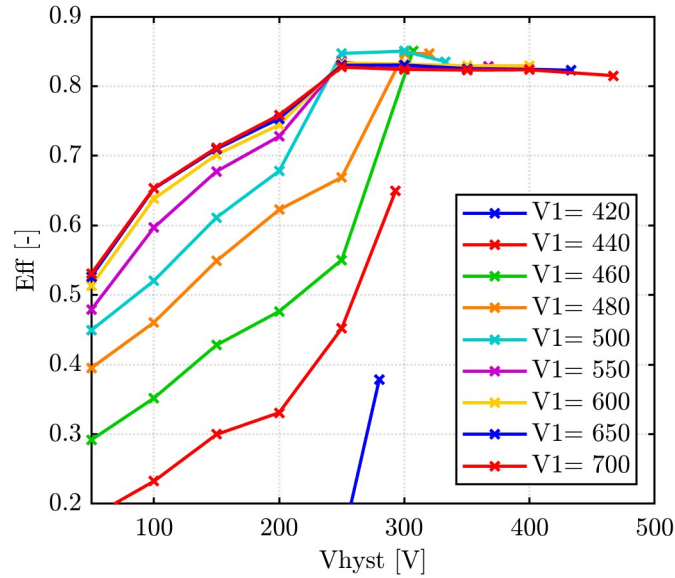


Figure 4.16: V_h and V_1 influence at 400V out with d control considering iron losses

The curves in Figure 4.16 show that at low hysteresis voltage values the efficiency decreases significantly. This phenomenon has been noted in experimental tests. From these results, it can be deduced that it is advantageous to work at hysteresis voltages as high as possible and to adjust the DC-link voltage of the inverter input to the electric motor. Another phenomenon that is useful to note is that the DC-link voltage needed for the efficiency to be high does not have to be as high as possible, as it would suggest the Figure 4.16. As the DC-link voltage increases the losses in the iron also increase limiting the efficiency. In this case, as can be seen from Figure 4.16, a higher DC-link voltage is not necessarily optimal.

In order to verify the effectiveness of this method of calculating iron losses, input and output powers and efficiency, some working points were considered for comparing the data of the laboratory with the results of the model. In Table 4.1 it is shown the data of the same working point that was considered for comparing the experimental and PLECS waveforms that is shown in Section 3.5 with an input voltage of 100V.

| | Experimental data | Simulation data (PLECS) | |
|-----------|--------------------------|--------------------------------|-----|
| P_{in} | 2179 | 2345 (1874) | [W] |
| P_{out} | 1928 | 1750 | [W] |
| P_{fe} | 77 | 166 | [W] |
| η | 88.5 | 74.6 | [-] |

Table 4.1: Results comparison $V_{in} = 100V$, $V_{out} = 70V$, $V_h = 60V$

In Table 4.2, on the other hand, a working point with an input voltage of 250V is tested.

| | Experimental data | Simulation data (PLECS) | |
|-----------|--------------------------|--------------------------------|-----|
| P_{in} | 3742 | 4050 (3297) | [W] |
| P_{out} | 2963 | 3165 | [W] |
| P_{fe} | 625 | 753 | [W] |
| η | 79.2 | 78 | [-] |

Table 4.2: Results comparison $V_{in} = 250V$, $V_{out} = 200V$, $V_h = 160V$

The results show an error concerning the calculation of iron losses, which depending on the operating point can be more or less pronounced, for example in Table 4.1 there is a large error because the loss data obtained from the fit for that value of magnetising current and frequency deviates from the experimental data. Generally, although not exactly, the simulation results express the behaviour of the converter well, as can be seen from the data shown in Table 4.2.

The map for calculating iron losses could be improved with a further campaign of experimental tests. For example, by carrying out new experimental tests at 560V input, since the data obtained at this voltage show the greatest discrepancies.

The model results proved to be good enough to represent the physical behaviour of the DC/DC stage verified in the laboratory with regard to the influence of the control parameters on the calculated powers and efficiency.

Chapter 5

Conclusions

The iOBC converter was especially studied with regard to the DC/DC stage, which is the innovative element that distinguishes it. The starting point was the control scheme and an initial PLECS model, but without prior knowledge of how this converter works. It was then contributed studying through a base theoretical model, experimentally and in simulation in order to better understand its operation. From the experimental tests, a first attempt was made to clarify how the various control parameters affect the charging power and efficiency. The data was also employed to correct and calibrate the PLECS model and make it as similar as possible to the real converter.

The experimental tests revealed issues that were not initially considered. One of these was the high current derivative due to the small inductance, which makes it difficult to control the current. Therefore to optimise the charging it was set the hysteresis current at 10A in order to reduce losses and focusing on the influence of the hysteresis voltage. Another problem, complicated by the high current derivative, concerns the q-axis component of the current. It is present even when trying to control it to zero via the q-axis control. A feed-forward component was added to the q-axis current control in order to reduce the cross-saturation effect.

From the experimental data, the model results were compared and modifications were made to the model to make it as close to reality as possible. The leakage inductance was measured and set into the model. The PECS control code was also corrected and improved in some parts. A PLECS script was written to automatically run the simulations by setting the different parameters from a table and save the desired data. It was then possible to conduct a simulation campaign in order to study the influence of the control parameters more in depth. The simulation campaign was useful as there are

several parameters that influence charging and relying exclusively on experimental data would have required an excessive number of tests.

The PLECS model does not consider iron losses but these were found to be largely relevant in the efficiency calculation. A method for calculating losses based on empirical data was therefore implemented. Iron losses are estimated by means of a fitting of the experimental data depending on the maximum magnetising current and its frequency. The iron losses calculated in this way are added to the electric motor input power obtained from the PLECS model and the efficiency is then recalculated. The method used is the same as the one PLECS uses when considering switch losses. In this way, significant power and efficiency trends were obtained which show well the physical behaviour of the converter. From the results obtained, it can be deduced how the converter can be controlled to obtain the desired power and the associated maximum efficiency.

A new method of controlling the battery charging current has been proposed and implemented. Based on the current error through a purely integral control, the hysteresis voltage command is generated. Using some approximations, the transfer functions of the current control loop were calculated. From the closed-loop transfer function, the integral gain of the controller was calculated in order to obtain the desired bandwidth. The system was tested in simulation and it was observed that it performed as desired.

This work has broadened the knowledge of how the converter actually works and has resulted in an improved control system and model. However, there are still a number of aspects that can be investigated in order to improve the converter and the model. From the new information known from the work carried out, a new experimental campaign could be conducted, choosing the various parameters specifically for what needs to be studied. For example, more data could be acquired in the sections where the OBC operates at high efficiency. From new experimental tests the fitting for the calculation of iron losses could also be improved. Regarding the control it would be necessary to research a new more effective methodology to try to minimise the q-axis current by working in feed forward. In addition, a new control could be investigated and tested experimentally to try to work at high efficiency. This could be achieved by maintaining the proposed battery current control but acting on the AFE for varying the dc-link voltage at the input of the electric motor. The dc-link voltage for maximum efficiency could be chosen by looking at new LUTs that could depend on the battery voltage information and the required charging power.

Bibliography

- [1] <https://www.iea.org/reports/global-ev-outlook-2022/trends-in-electric-light-duty-vehicles/>
- [2] <https://www.irena.org/publications/2019/Apr/Global-energy-transformation-A-roadmap-to-2050-2019Edition/>
- [3] <https://iea.blob.core.windows.net/assets/ad8fb04c-4f75-42fc-973a-6e54c8a4449a/GlobalElectricVehicleOutlook2022.pdf/>
- [4] <https://energy.mit.edu/wp-content/uploads/2019/11/Insights-into-Future-Mobility.pdf/>
- [5] <https://www.un.org/en/climatechange/paris-agreement>
- [6] <https://www.consilium.europa.eu/en/policies/green-deal/>
- [7] European Roadmap Electrification of Road Transport, 3rd Edition, Version: 10, June 2017.
- [8] <https://www.bp.com/content/dam/bp/business-sites/en/global/corporate/pdfs/energy-economics/statistical-review/bp-stats-review-2021-full-report.pdf>
- [9] <https://www.volkswagen-newsroom.com/en/modular-electric-drive-matrix-meb-3677>
- [10] <https://www.bosch-mobility-solutions.com/en/solutions/powertrain/vehicle-platforms/advanced-driving-module/>
- [11] <https://fitgen-project.eu/>
- [12] K. Fahem, D. E. Chariag, and L. Sbita, “On-board bidirectional battery chargers topologies for plug-in hybrid electric vehicles” in Proc. Int. Conf. Green Energy Convers. Syst. (GECS), Mar. 2017, pp. 1–6.

- [13] M. Martino, P. Pescetto and G. Pellegrino, "Advanced Functionally Integrated E-Axle for A-Segment Electric Vehicles," 2020 AEIT International Conference of Electrical and Electronic Technologies for Automotive (AEIT AUTOMOTIVE), 2020, pp. 1-6, doi: 10.23919/AEITAUTOMOTIVE50086.2020.9307382.
- [14] M. Valente, T. Wijekoon, F. Freijedo, P. Pescetto, G. Pellegrino and R. Bojoi, "Integrated On-Board EV Battery Chargers: New Perspectives and Challenges for Safety Improvement," 2021 IEEE Workshop on Electrical Machines Design, Control and Diagnosis (WEMDCD), 2021, pp. 349-356, doi: 10.1109/WEMDCD51469.2021.9425666.
- [15] M. Y. Metwly, M. S. Abdel-Majeed, A. S. Abdel-Khalik, R. A. Hamdy, M. S. Hamad and S. Ahmed, "A Review of Integrated On-Board EV Battery Chargers: Advanced Topologies, Recent Developments and Optimal Selection of FSCW Slot/Pole Combination," in IEEE Access, vol. 8, pp. 85216-85242, 2020, doi: 10.1109/ACCESS.2020.2992741.
- [16] H. Karneddi, D. Ronanki and R. L. Fuentes, "Technological Overview of Onboard Chargers for Electrified Automotive Transportation," IECON 2021 – 47th Annual Conference of the IEEE Industrial Electronics Society, 2021, pp. 1-6, doi: 10.1109/IECON48115.2021.9589679.
- [17] E. A. Grunditz and T. Thiringer, "Performance Analysis of Current BEVs Based on a Comprehensive Review of Specifications," in IEEE Transactions on Transportation Electrification, vol. 2, no. 3, pp. 270-289, Sept. 2016, doi: 10.1109/TTE.2016.2571783.
- [18] P. Pescetto and G. Pellegrino, "Isolated On-Board Battery Charger Integrated with 6-phase Traction Drive," 2020 23rd International Conference on Electrical Machines and Systems (ICEMS), 2020, pp. 309-314, doi: 10.23919/ICEMS50442.2020.9290958.
- [19] P. Pescetto and G. Pellegrino, "Isolated Semi Integrated On-board Charger for EVs Equipped with 6-phase Traction Drives," IECON 2021 – 47th Annual Conference of the IEEE Industrial Electronics Society, 2021, pp. 1-6, doi: 10.1109/IECON48115.2021.9589656.
- [20] M. Yilmaz and P. T. Krein, "Review of Battery Charger Topologies, Charging Power Levels, and Infrastructure for Plug-In Electric and Hybrid Vehicles," in IEEE Transactions on Power Electronics, vol. 28, no. 5, pp. 2151-2169, May 2013, doi: 10.1109/TPEL.2012.2212917.

- [21] I. Subotic et al., “Isolated chargers for EVs incorporating six-phase machines,” 653–664 63 IEEE Trans. Ind. Electron., 2015.
- [22] S. Haghbin et al., “An isolated high-power integrated charger in electrified-vehicle applications,” 4115–4126 60 IEEE Trans. Veh. Technol., 2011.
- [23] A. S. Abdel-Khalik et al., “Interior permanent magnet motor-based isolated on-board integrated battery charger for electric vehicles,” 124–134 12 IET Electr. Power Appl., 2017.
- [24] P. Pescetto et al., “Integrated isolated obc for EVs with 6-phase traction motor drives,” in 2020 IEEE Energy Conversion Congress and Exposition (ECCE). 4112–4117 IEEE, 2020
- [25] D. Thimmesch, “An SCR inverter with an integral battery charger for electric vehicles,” 1023–1029 IEEE Trans. Ind. Appl., 1985
- [26] T. Na et al., “A review of on-board integrated electric vehicles charger and a new single-phase integrated charger,” 288–298 4 CPSS Transactions on Power Electronics and Applications, 2019.
- [27] W. E. Rippel et al., “Integrated motor drive and recharge system,” Mar. 24 1992, uS Patent 5,099,186.
- [28] S.-K. Sul et al., “An integral battery charger for four-wheel drive electric vehicle,” 1096–1099 31 IEEE Trans. Ind. Appl., 1995.
- [29] G. Pellegrino et al., “An integral battery charger with power factor correction for electric scooter,” 751–759 25 IEEE transactions on power electronics, 2009.
- [30] S. Loudot et al., “Fast charging device for an electric vehicle,” Sep. 30 2014, uS Patent 8,847,555.
- [31] L. Shao et al., ” 116900–116913 8 “Design approaches and control strategies for energy-efficient electric machines for electric vehicles—a review, 2020.
- [32] M. S. Diab et al., “A nine-switch-converter-based integrated motor drive and battery charger system for EVs using symmetrical six-phase machines,” 5326–5335 63 IEEE Trans. Ind. Electron., 2016.

- [33] L. De Sousa et al., “Method and electric combined device for powering and charging with compensation means,” Oct. 6 2015, uS Patent 9,153,996.
- [34] I. Subotic et al., “Onboard integrated battery charger for EVs using an asymmetrical nine-phase machine,” 3285–3295 62 IEEE Transactions on industrial electronics, 2014.
- [35] E. Agamloh et al., “An overview of electric machine trends in modern electric vehicles,” 20 8 Machines, 2020.
- [36] A. M. El-Refaie, “Motors/generators for traction/propulsion applications: A review,” 90–99 8 IEEE Veh. Technol. Mag., 2013.
- [37] Z.-Q. Zhu et al., “Electrical machines and drives for electric, hybrid, and fuel cell vehicles,” 746–765 95 Proc. IEEE, 2007.
- [38] I. Subotic et al., “An ev drive-train with integrated fast charging capability,” 1461–1471 31 IEEE Trans. Power Electron., 2015.
- [39] S. Foti et al., “An integrated battery charger for ev applications based on an open end winding multilevel converter configuration,” in 2019 21st European Conference on Power Electronics and Applications (EPE’19 ECCE Europe). P–1 IEEE, 2019.
- [40] S. Semsar et al., “Integrated single-phase electric vehicle charging using a dual-inverter drive,” in 2018 IEEE Transportation Electrification Conference and Expo (ITEC). 320–325 IEEE, 2018.
- [41] I. Subotic et al., “Integration of six-phase EV drivetrains into battery charging process with direct grid connection,” 1012–1022 32 IEEE Trans. Energy Convers., 2017.
- [42] Massimiliana Carello, Henrique de Carvalho Pinheiro, Leonardo Longega, Luca Di Napoli, *Design and Modelling of the Powertrain of a Hybrid Fuel Cell Electric Vehicle*. SAE Technical Paper 2021-01-0734; SAE International: Warrendale, PA, USA, 2021.